https://ntrs.nasa.gov/search.jsp?R=20180000518 2019-04-30T04:20:27+00:00Z

Comparisons Between NO PLIF Imaging and CFD Simulations of Mixing Flowfields for High-Speed Fuel Injectors

Tomasz G. Drozda,[†] Karen F. Cabell,[†] Austin R. Ziltz,[‡] Neal E. Hass,[†]
Hypersonic Airbreathing Propulsion Branch, NASA Langley Research Center, Hampton, VA, 23681
Jennifer A. Inman,[†] Ross A. Burns,[§] Brett F. Bathel,[†] Paul M. Danehy,[¶]
Advanced Measurement and Data Systems Branch, NASA Langley Research Center, Hampton, VA, 23681

ABSTRACT

The current work compares experimentally and computationally obtained nitric oxide (NO) planar laser-induced fluorescence (PLIF) images of the mixing flowfields for three types of high-speed fuel injectors: a strut, a ramp, and a rectangular flushwall. These injection devices, which exhibited promising mixing performance at lower flight Mach numbers, are currently being studied as a part of the Enhanced Injection and Mixing Project (EIMP) at the NASA Langley Research Center. The EIMP aims to investigate scramjet fuel injection and mixing physics, and improve the understanding of underlying physical processes relevant to flight Mach numbers greater than eight. In the experiments, conducted in the NASA Langley Arc-Heated Scramjet Test Facility (AHSTF), the injectors are placed downstream of a Mach 6 facility nozzle, which simulates the high Mach number air flow at the entrance of a scramjet combustor. Helium is used as an inert substitute for hydrogen fuel. Both schlieren and PLIF techniques are applied to obtain mixing flowfield flow visualizations. The experimental PLIF is obtained by using a UV laser sheet to interrogate a plane of the flow by exciting fluorescence from the NO molecules, which are present in the AHSTF air. Consequently, the absence of signal in the resulting PLIF images is an indication of pure helium (fuel). The computational PLIF is obtained by applying a fluorescence model for NO to the results of the Reynolds-averaged simulations (RAS) of the mixing flowfield carried out using the VULCAN-CFD solver. This approach is required because the PLIF signal is a nonlinear function of not only NO concentration, but also pressure, temperature, and the flow velocity. This complexity allows additional flow features to be identified and compared with those obtained from the computational fluid dynamics (CFD) simulations, however, such comparisons are only semiquantitative. Three-dimensional image reconstruction, similar to that used in magnetic resonance imaging, is also used to obtain images in the streamwise and spanwise planes from select cross-stream PLIF plane data. Synthetic schlieren is also computed from the RAS data. Good agreement between the experimental and computational results provides increased confidence in the CFD simulations for investigations of injector performance.

Statement A: Approved for public release; distribution is unlimited.

[†] Research Aerospace Engineer.
[‡] Research Engineer, ACEnT Labs.
[§] Research Engineer, National Institute of Aerospace.
[¶] NASA Langley Senior Technologist.

INTRODUCTION

Flight demonstrations of hypersonic air-breathing vehicles[1,2] prove their increasing promise for military (rapid response and strike capability on a global scale), aerospace (safer and more affordable access to space), and civil aviation (hypersonic point-to-point transport) applications. However, designing supersonic combustion ramjet (scramjet) engines capable of robust air-breathing operation, characterized by rapid fuel-air mixing and short combustion times while ensuring flame stability and high combustion efficiency over a wide range of speeds, has proven difficult. Attempts at improving fuel injection to enhance fuel-air mixing while simultaneously reducing propulsive losses have received a great deal of attention over the years, as summarized by Lee et al.[3] Although some total pressure loss is thermodynamically unavoidable and occurs due to the desired effect of molecular mixing of the fuel and air, any losses beyond this minimum required amount reduce the thrust potential of the engine.

The Enhanced Injection and Mixing Project (EIMP), being executed at the NASA Langley Research Center, represents an effort to achieve more rapid mixing at high speeds.[4] The EIMP aims to investigate scramjet fuel injection and mixing physics, improve the understanding of underlying physical processes, and develop enhancement strategies relevant to flight Mach numbers greater than eight. The experiments, which are underway in the Arc-Heated Scramjet Test Facility (AHSTF), utilize a Mach 6 facility nozzle to simulate a nondistorted combustor entrance flow of a scramjet engine. The fuel injectors tested to date consist of a fuel placement device (strut), a fluidic vortical mixer (ramp), and a high aspect ratio rectangular flushwall injector. These devices accomplish the necessary task of distributing and mixing fuel into the supersonic crossflow, albeit via different strategies. These devices were previously studied at lower flight Mach numbers where they exhibited promising performance in terms of mixing efficiency and total pressure recovery.[5,6] Computational fluid dynamics (CFD) simulations, and the corresponding comparative analysis of these injectors under the current conditions of interest, were also previously investigated.[7]

The EIMP experiments include quantitative in-stream measurements as well as flow visualization of the mixing flowfield via schlieren and the nitric oxide (NO) planar (P) laser-induced fluorescence (LIF) technique, or NO PLIF. The present work takes advantage of the fact that NO naturally exists in low concentrations in the facility air[8] as a result of the electric-arc heating process. The NO acts as an in situ flow tracer that can be imaged using PLIF. NO PLIF uses an ultraviolet (UV) laser sheet to illuminate a planar slice in the flow. The UV light excites fluorescence from the NO molecules, which is detected by a digital camera. The PLIF technique has been employed in numerous supersonic fuel-air mixing studies.[9–17] The present application follows closely the method of Fox et al.,[13] where NO is in the air stream instead of the fuel (helium) stream, thus the absence of signal is an indication of pure fuel and the intensity of the fluorescence is proportional to the concentration of NO. Because the instantaneous concentration of NO is not precisely known or controlled, this experimental approach presents a unique set of challenges from those where a known amount of NO is seeded into the flow. Furthermore, the measured NO PLIF signal is also sensitive to pressure and temperature variations, both of which can vary significantly in a compressible flow with shock and expansion features. Nevertheless, the current approach is similar to the previous work of Fox et al.,[13] and Gaston et al.[14]

Prior to conducting mixing tests, earlier experiments were conducted in the AHSTF with the laser sheet configured to interrogate the flow at the exit of the Mach 6 facility nozzle.[18] These tests confirmed that NO exists in the AHSTF air in sufficient concentration (i.e., to produce enough fluorescence to detect) and sufficient spatial uniformity for images obtained from the mixing flowfield to be interpreted properly (i.e., concentration of NO proportional to concentration of air). The current work describes an initial set of qualitative mixing tests of the injectors described above using only flow visualizations and no quantitative in-stream measurements. The flow visualization consisted primarily of NO PLIF imaging along both streamwise and cross-stream flow planes. However, schlieren was also used for a small subset of tests to investigate the usefulness of this technique for the mixing experiments.

The experimental visualization data are also compared with the same quantities obtained from the numerical simulations. Computing experimentally-equivalent visualization from the CFD is referred to as computational flow imaging (CFI).[19] The CFI for PLIF is obtained by applying a fluorescence model for NO[20] to the results of the Reynolds-averaged simulations (RAS) obtained using the VULCAN-CFD solver.[21] To obtain CFI for the schlieren, termed synthetic schlieren, the simulation results are used to evaluate density gradients in the relevant direction. The resulting images are the computational equivalent to the experimentally obtained schlieren and PLIF visualizations. Although CFI promises to make direct comparisons with the available experimental data, quite often, due to uncertainties associated with modeling physical processes, and application of complex, nonlinear, data postprocessing techniques, the comparisons between experimental visualizations and CFI are only semiquantitative. Nevertheless, good agreement between the experimental visualizations and CFI provides increased confidence in the CFD simulations and the corresponding CFD analysis of the injector performance (e.g., Drozda et al.[7]).

This paper first describes the mixing experiments, injector geometries, flow conditions, and the corresponding CFD simulations. Only relevant highlights of the CFD results are presented here to give the reader a qualitative understanding of the flowfield and the performance generated by each injector geometry. The primary focus of the paper is the experimental setup, execution, and data postprocessing of the schlieren and NO PLIF, as well as the details of the CFI for both. Finally, the results of the experimental and computational visualizations are compared and discussed.

MIXING EXPERIMENTS

EIMP experiments entail testing various fuel injection devices mounted on an open flat plate located downstream of a Mach 6 facility nozzle, which simulates the combustor entrance of a flight vehicle traveling at a Mach number of about 14 to 16. The open flat plate is used because it facilitates optical access to the fuel-air mixing region. Figure 1 shows an isometric view of the AHSTF test cabin with the bulkhead and facility nozzle removed to reveal the test section and the experimental apparatus. The test section is 4 ft in diameter. The test cabin has four doors that provide both physical and optical access to the test section. In the current experiments, the two doors adjacent to the open flat plate have windows and are used for the optical access for schlieren and PLIF imaging. The figure also shows the orientation of the experimental article (i.e., the flat plate with a row of fuel injectors installed) as it is installed in the AHSTF test cabin. The x, y, and z axes denote the streamwise, spanwise, and cross-stream coordinate directions, respectively.

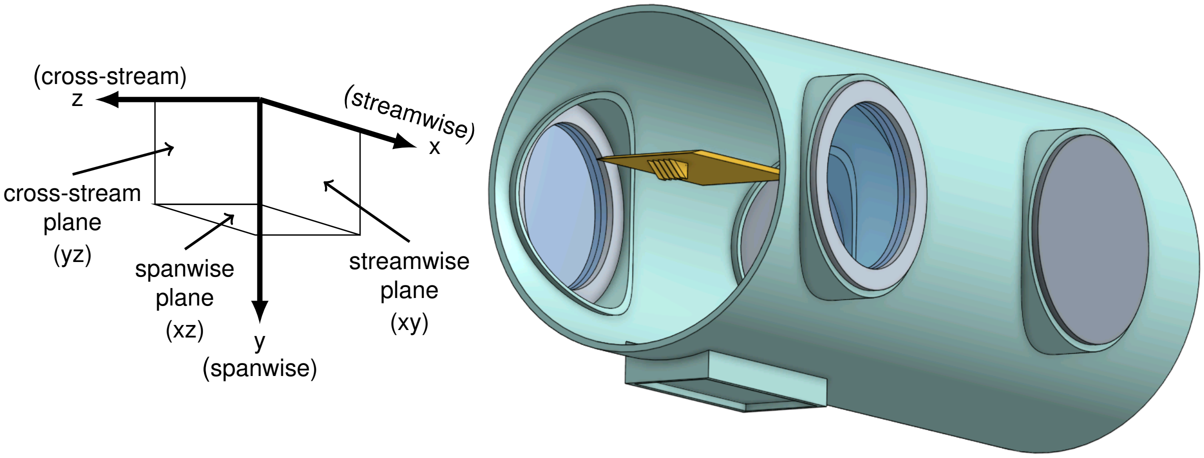

Figure 1. Isometric view of the AHSTF facility test cabin with the bulkhead and facility nozzle removed to reveal the notional position of the open flat plate with the strut injector block installed. The facility air flow is along the x-axis.

It should be noted that in the current work, the positive spanwise dimension (along the y-axis) is oriented in the flat plate normal direction, which in this figure is pointing toward the ground. Furthermore, in the discussions that follow, the streamwise, cross-stream, and spanwise planes correspond to the xy-, yz-, and the xz-planes, respectively. The facility air flow is along the x-axis.

Figure 2 shows a cross-sectional view of the test cabin and the experimental apparatus. Noted on the figure is the flat plate with its leading edge positioned 2.5 inches below the top wall of the 10 inch by 10 inch Mach 6 facility nozzle. The flow is from left to right. The flat plate is 28.87 inches long tip-to-tail, 32 inches wide, and features a rectangular opening for mounting interchangeable injector blocks. The trailing edge of the injector block is located 8.87 inches downstream of the flat plate leading edge. In the current work, this location is the origin of the x-axis, with the origin of the y-, and z-axes located at the center along the width, and on the surface of the flat plate. The injector blocks, in general, can accommodate a spanwise row of several injectors. The facility air flows over the injector bodies and mixes with the fuel simulant (helium) downstream of the injection plane. Also noted in Fig. 2 are the in-stream rake traverse system (used for pitot pressure, total temperature, and gas sampling probes), the jet stretchers (designed to prevent over- and underexpansion of the facility air flow over the mixing region), and the instrumentation shroud located on the upper side of the flat plate. In the current experiments, neither the in-stream rake traverse nor the jet-stretchers are installed. Further details about the experimental setup and EIMP are presented in Cabell et al.[4] The experiment is intended to provide a test-bed for rapidly testing a variety of different fuel injector devices and injection strategies. Current experiments focus on studying fuel injection and mixing processes in the absence of heat release by utilizing helium as a fuel simulant. Furthermore, these experiments are referred to as "cold flow" because the range of air total temperatures is significantly lower than the relevant flight total temperature. The low end of the range is bounded by the condensation limit for the expanding facility air and the high end by the thermal-structural limits of the uncooled hardware. The former and latter correspond to 728 K and 978 K, respectively. However, the Reynolds numbers are comparable between the ground experiments and the notional flight condition. Only the upper limit of the total temperature is included in the current study of the EIMP case because previous work[22] has shown that the results obtained for the lower limit are similar.

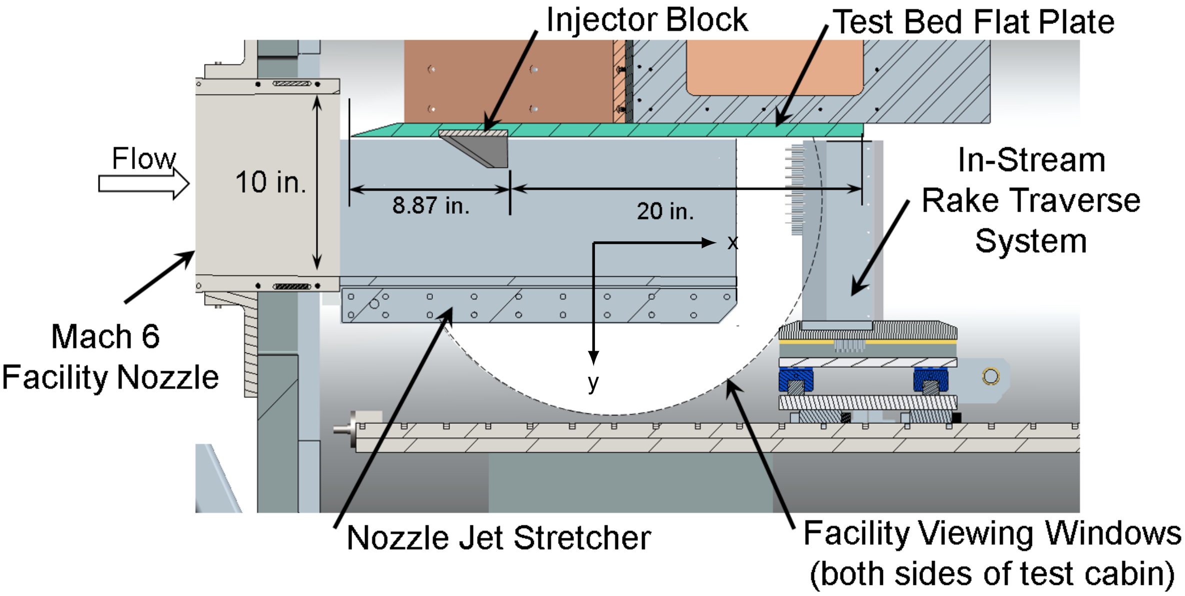

Figure 2. Cross-sectional view the experimental cabin showing the facility nozzle, flat plate, injector block, jet-stretchers, instrumentation shroud (above the flat plate), and the in-stream rake system. The facility viewing window is denoted by a dashed line.

Table 1. Nominal global parameters of interest for the strut, ramp, and flushwall injector configurations. The last set of rows contain ratios of interest between the fuel (helium) and air streams, where the subscripts f and a denote fuel and air streams, respectively.

Property	Air[†]	Strut	Ramp	Flushwall
Mach	6.36	2.98	2.96	2.98
$P0$ (MPa)	4.309	0.224	0.0882	0.424
$T0$ (K)	977.8	293.15	293.15	293.15
P (kPa)	1.808	7.205	2.911	13.642
T (K)	112.4	74.14	74.91	74.14
u (m/s)	1353	1508	1505.6	1508.2
Re' (1/in) x10e3	259.4	358.4	143.1	678.6
$\dot{\mathrm{m}}_{\mathrm{a}}$ (kg/s) x10e-3		98.76	65.84	187.00
$\dot{\mathrm{m}}_{\mathrm{f}}$ (kg/s) x10e-3		2.884	1.922	5.460
$\Delta\mathrm{U}$[‡]		0.054	0.054	0.054
$\mathrm{M_c}$[§]		0.22	0.21	0.22
$\rho_{\mathrm{f}} \,/\, \rho_{\mathrm{a}}$		0.84	0.33	1.58
$\mathrm{p_f} \,/\, \mathrm{p_a}$		3.98	1.61	7.54
J[¶]		1.04	0.42	1.97

[†] 21% $\mathrm{O_2}$, 78% $\mathrm{N_2}$, 1% NO

[‡] Velocity difference parameter, $\Delta U = (u_f - u_a)/(u_f + u_a)$

[§] Convective Mach number, $M_c = |u_f - u_a|/(c_f + c_a)$, c denotes the speed of sound.

[¶] Dynamic pressure ratio, $J = (\rho_f u_f^2)/(\rho_a u_a^2)$.

NOMINAL FLOW CONDITIONS AND INJECTOR GEOMETRIES

The nominal facility air conditions correspond to a total pressure and total temperature of 4.31 MPa (625 psi) and 978 K (1760 °R), respectively, expanded to a Mach number of 6.4.[23] A nonreacting, thermally perfect mixture of 21% oxygen (O_2), 78% nitrogen (N_2), and 1% nitric oxide (NO) by volume was assumed for the air.[8] The fuel mass flow rate of helium for each injector was computed by assuming an equivalence ratio (ER) of one over the "intended" fueling area as if it were fueled with hydrogen. The intended fueling areas for the strut and ramp are portions of the cross-sectional area of the complete combustor flowpath that are intended to be fueled by a single injector with the ER of one. For the strut and ramp injectors, the intended fueling areas were obtained from Baurle et al.,[5] who considered them in a realistic scramjet combustor configuration. The values of several flow parameters are shown in Table 1. The properties of both the air and the fuel are presented. The subscripts 0, f, and a denote total conditions, fuel, and air flow streams, respectively. It should be noted that these values correspond to the nominal conditions used in, or obtained from, the CFD simulations. The quantities that were measured experimentally varied slightly from run-to-run from the nominal values. The following nondimensional quantities are also shown: the unit Reynolds number per inch for the air and fuel streams, Re'; velocity difference parameter, $\Delta\mathrm{U}$; the convective Mach number, $\mathrm{M_c}$; the ratios of the density, $\rho_{\mathrm{f}} \,/\, \rho_{\mathrm{a}}$, and static pressure, $\mathrm{p_f} \,/\, \mathrm{p_a}$; and dynamic pressure, J, between the fuel and air stream. All values are computed based on the combustor entrance flow conditions for the air and the expanded flow conditions at the exit of the injector ports for the fuel. These nondimensional quantities have been found to be relevant to the injection and mixing processes in canonical problems.[24–26]

As stated earlier, the three types of injectors investigated in the current study are a strut, a ramp, and a flushwall injector. The same strut and ramp have been previously studied by Baurle et al.[5] under "cold" flow conditions at a combustor entrance Mach number of 4.5. However, unlike the experiments and simulations discussed in Baurle et al.,[5] which configured the injectors in a closed duct and interdigitated fashion, the current work includes a row of injectors on an open flat plate. The flushwall injector is a rectangular, high-aspect ratio design based on the optimization work of Ogawa[6] at Mach 5.7 flow conditions. Although the computational simulations included a row of flushwall injectors, only a single injector was able to be accommodated in the current experiments.

The first injector is a slender swept strut protruding into the flow. Strut injectors have several advantages in hypervelocity flow applications. First, they can be designed to place the fuel where it is needed, thereby alleviating the need to consider fuel penetration issues and focusing only on the injector spacing. Second, the injector ports on a strut are typically aligned parallel to the flow, which allows the injected fuel streams to augment the thrust of the engine. The potential downsides of a strut injector are the structural integrity and cooling requirements needed for its slender body, the drag (both viscous and pressure) that it induces on the flow by the obstruction it generates, and the total pressure loss incurred by the oblique shocks that emanate from its body. Views and dimensional details of the strut are shown in Fig. 3. In the current simulations and experiments, the distance between adjacent strut injectors is 0.9 inches. Each injector port has a throat diameter of 0.083 inches followed by a conical expansion with a half-angle of 6 degrees that is designed to expand helium to a Mach number of about 3.

The second injector is an unswept ramp. Compared to the strut, the ramp injector does not protrude as far into the flow. The ramp injector generates a counter-rotating vortex pair (CVP) with one vortex on each side of the ramp as the flow passes over the ramp and through the gaps between the ramps, which convects the injected fuel upward, toward the core of the flow. In addition to inducing the upward entrainment, the CVP stretches the fuel-air interface thereby increasing the surface area over which the turbulence and the molecular viscosity can act to mix the fuel and air. Because the strength of the CVP depends on both the geometry of the ramp and the incoming air flow conditions, designing an injector that robustly fills its intended fueling area across a range of flight conditions is more challenging for a ramp than a strut. As with the strut, the ports of the ramp injector are also nearly aligned parallel to the flow and allow for injected fuel streams to augment the thrust of the engine. However, the ports are angled slightly upward and to the side to aid in directing the fuel streams toward the CVP. The ramp injector also generates an oblique

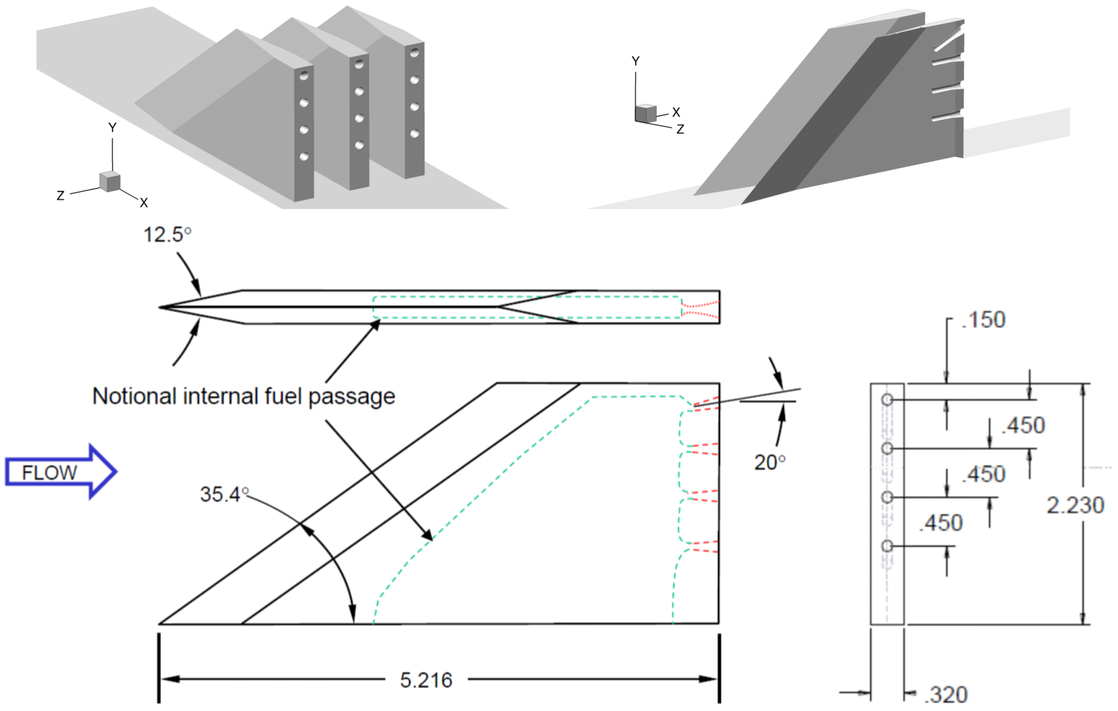

Figure 3. Isometric views and dimensional details of the baseline strut injector. Linear dimensions are in inches.

shock due to its inclined surface. Views of the ramp, and its dimensional details are shown in Fig. 4. In the current simulations, the distance between adjacent ramps is 1.2 inches. This spacing is also the same as that found between the interdigitated ramp configuration of Baurle et al.[5] Each injector port has a throat diameter of 0.108 inches followed by a conical expansion with a half-angle of 10 degrees that is designed to expand helium to a Mach number of about 3.

The third injector is a high-aspect-ratio rectangular flushwall injector. Unlike the strut and ramp, the flushwall injector introduces no physical blockage into the flow. Instead, a number of flow features form around the injection site that interact to produce a similar effect. These features are shown schematically for a generic round flushwall injector in Fig. 5. The bow shock that forms upstream of the injection plume creates both total pressure losses and aerodynamic blockage by forcing the air stream to flow around the fuel plume. As is the case for the ramp injector, the fuel plume entering the high-speed crossflow generates a CVP, which

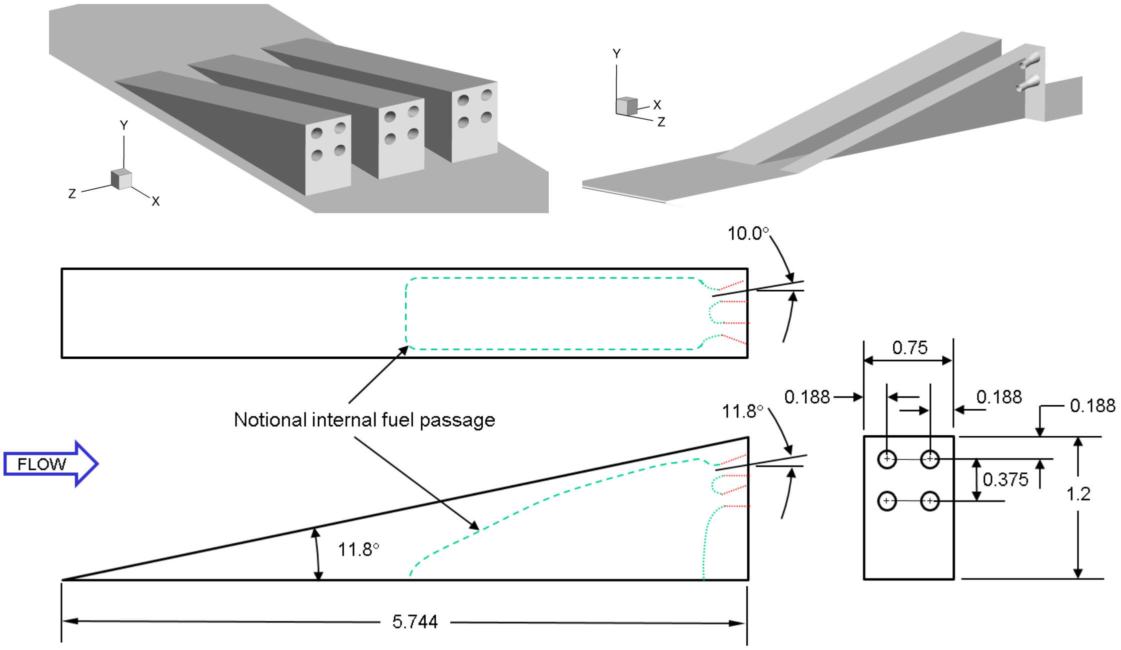
Y
Z
X
Y
X
Z
10.0°
Notional internal fuel passage
FLOW
11.8°
0.75
0.188
0.188
0.188
0.375
1.2
11.8°
5.744

Figure 4. Isometric views and dimensional details of the baseline ramp injector. Dimensions are in inches.

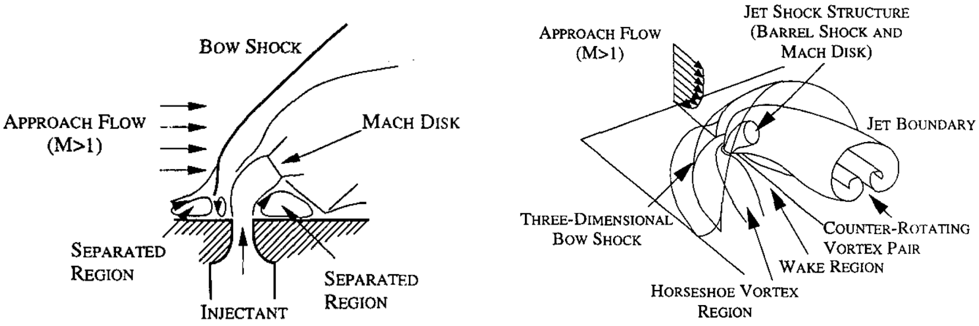
Bow Shock
Approach Flow
(M>1)
Mach Disk
Separated
Region
Injectant
Separated
Region
Approach Flow
(M>1)
Jet Shock Structure
(Barrel Shock and
Mach Disk)
Jet Boundary
Three-Dimensional
Bow Shock
Counter-Rotating
Vortex Pair
Wake Region
Horseshoe Vortex
Region

Figure 5. Side and isometric views of the flow features that form around a generic flushwall injector during transverse injection of fuel into the supersonic cross-stream. From Gruber et al.[27]

becomes the main mechanism for stirring the fuel into the air. However, unlike a fuel placement device, such as a strut, the extent to which the fuel penetrates into the air flow is governed by fluidic considerations.[3,28–30] The jet penetration has been shown to be primarily proportional to the dynamic pressure (or momentum flux) ratio, J, between the main air and the fuel jet, and is further enhanced by matching the static pressure at the exit of the fuel injector to the effective static pressure, that is, the static pressure of the air just upstream of the fuel plume and downstream of the bow shock. Penetration also increases with the increasing thickness of the approach boundary layer[31] due to aerodynamic "shielding," that is, the lower momentum of the boundary layer effectively increases the dynamic pressure ratio, which leads to the increases in the jet penetration by an amount typically greater than the boundary layer thickness.

The flushwall injector exit geometry is based on the multiobjective optimization work of Ogawa[6] whose approach using a genetic algorithm revealed four families of high performing flushwall injectors. The injector port chosen for the current work has a constant width, rectangular cross-section, with an aspect ratio of 8 at the injector exit plane, and the longer dimension aligned in the streamwise direction. The injector is also inclined at 30 degrees to the wall. Several views, and dimensional details of the flushwall injector are shown in Fig. 6. The injector has been further designed to qualitatively match the geometrical features of the fuel ports of the strut injector. As such, each flushwall injector port contains an expansion section with a 6 degree half-angle, and an expansion area ratio matching that of the strut conical fuel port. The area at the end of the expansion section, but before the 30-degree rotation (denoted by a 0.4551 dimension), has been adjusted to match the total exit area of the 4 fuel ports of the strut. The width of the injector is 0.1392 inches with a throat height of 0.1541 inches. In the CFD simulations, the distance between adjacent flushwall injectors is 1.704 inches, however, the experimentally tested flushwall injector block contains only a single

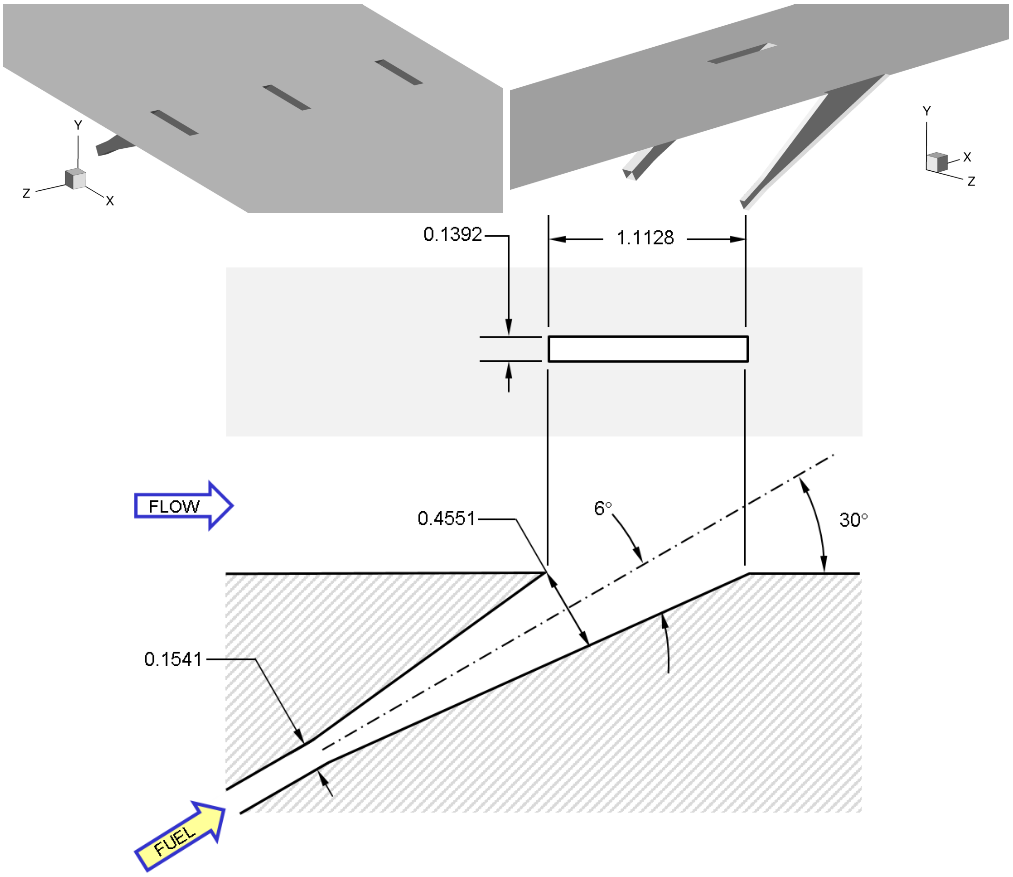

Figure 6. Isometric views and dimensional details of the baseline flushwall injector.

injector. The spacing corresponds to about 6 times the diameter of a circular injector with an equivalent area, and about 1.5 times the length of the current injector, allowing for a sufficient air-gap between the adjacent injectors even after the expected axis-switching of the fuel plume.[6]

COMPUTATIONAL MODELING

The numerical simulations were performed using the Viscous Upwind aLgorithm for Complex flow ANalysis (VULCAN-CFD) code.[21] VULCAN-CFD is a multiblock, structured-grid, cell-centered, finite-volume solver widely used for all-speed flow simulations. For this work, RAS were performed. The advective terms were computed using a Monotonic Upstream-Centered Scheme for Conservation Laws (MUSCL) scheme[32] with the Low-Dissipation Flux-Split Scheme (LDFSS) of Edwards.[33] The thermodynamic properties of the mixture components were computed using curve fits of McBride et al.[34] The governing equations were integrated using an implicit diagonalized approximate factorization (DAF) method.[35] The current work used the baseline blended $\mathrm{k}-\omega/\mathrm{k}-\epsilon$ turbulent physics model of Menter.[36] The Reynolds heat and species mass fluxes were modeled using a gradient diffusion model with turbulent Prandtl and Schmidt numbers of 0.9 and 0.5, respectively. These values were set based on experience and best practice with similar flows. Wilcox wall matching functions[37] were also used, however, their implementation in VULCAN-CFD includes a modification that allows the simulations to recover the integrate-to-the-wall behavior as the value of normalized wall-distance, y+, approaches one. All simulations were converged until the total integrated mass flow rate and the total integrated heat flux on the walls remained constant to within six significant digits. This typically occurred when the value of the L_2-norm of the steady-state equation-set residual decreased by about 4–5 orders of magnitude. Grid dependence analyses for the numerical simulations of both the strut and ramp injectors were previously assessed by Drozda et al.[7] The numerical simulations took advantage of the geometric symmetries of the injectors, therefore, only a single injector is simulated with the symmetry boundary conditions used at the midplane between the adjacent injectors. It should also be noted that all of the CFD simulations were performed pretest, and no attempt was made to rerun the simulations to match the experimental flow conditions (e.g., total pressure and temperature, Mach number, and ER) exactly.

Contour plots of the Mach number in the streamwise planes obtained through the center of the injector ports and midway between the injectors, and in cross-stream at various locations for the strut, ramp, and the flushwall injectors are shown in Figs. 7–9, respectively. For the cross-stream planes, the aspect ratio is not equal to one because these planes are viewed looking aft-to-fore from an angle of about 30 degrees to the x-axis. The streamwise distance on these figures is in inches. The black isocontour line denotes a helium mass fraction equal to the stoichiometric value for hydrogen (0.0285).

Qualitatively, the flow features for all of the injectors are very similar. Upstream, the leading edge of the flat plate causes a shallow bow shock at about 12.5 degrees to the flat plate, which is slightly larger than the Mach wave angle of about 9 degrees for this Mach number. For the strut injector, shown in Fig. 7, a cross-stream shock wave is generated by the sharp leading edge of the strut injector body (e.g., at -3 inches). The turning half-angle of the strut injector body leading edge is 6.25 degrees (see Fig. 3) in the horizontal xz-plane, resulting in the leading edge shock wave angle of about 17 degrees as measured from the CFD in the same plane. Because the leading edge of the strut body is swept at 35.4 degrees, the resulting oblique shock wave forms at a somewhat larger angle than that expected for the turning angle of 6.25 degrees. This shock wave propagates in the cross-stream direction and impacts the body of the adjacent injector. This propagation is evident by the change in the value of the Mach number at downstream locations between -3 and 0 inches on the middle plots of each figure. After the reflection from the adjacent injector, the oblique shock waves continue to pass through one another and interact, leading to the complex downstream pattern seen in the figures. As the flow continues past the strut injector body, a CVP forms near the tip of the injector body. The top-most fuel port injects the fuel stream directly into the space between the CVP. The combined effect of the angled injection and the CVP distorts and bifurcates the top-most fuel stream, and separates

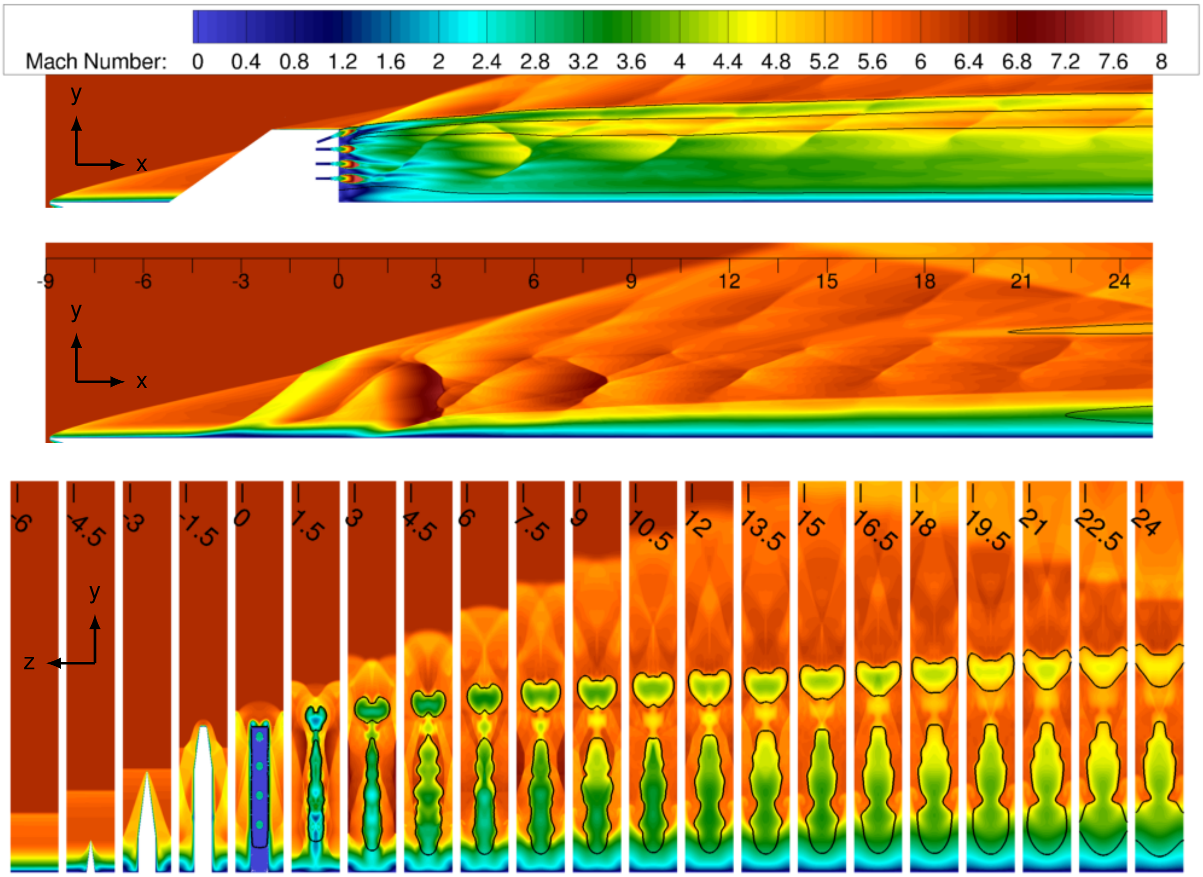

Figure 7. Contours of the Mach number on the streamwise planes obtained at the centerline, and half-way between the injectors, and cross-stream planes at various downstream locations for strut injector CFD simulations. Downstream distance is in inches. Black lines denote the stoichiometric value of the fuel mass fraction.

it from those of the three lower parallel fuel ports. This effect can be seen by observing the stoichiometric value of the fuel mass fraction as it evolves in the cross-stream planes in Fig. 7.

For the ramp injector, shown in Fig. 8, an oblique shock wave is generated by the inclined ramp surface of the ramp injector body. The turning angle of the ramp surface is 11.8 degrees (see Fig. 4), resulting in the oblique shock wave angle of about 17 degrees at the injector centerline. The value of this angle is slightly reduced from the expected value (of about 19 degrees) for this turning angle because of the interaction of the shock with the approach boundary layer, resulting in a small separation bubble forming just upstream of the ramp. This oblique shock interacts and coalesces with the same shock wave produced by the adjacent injector bodies. However, unlike the cross-stream shock waves that emanate from the leading edge of the strut, the ramp body oblique shock wave does not interact with the fuel-air mixing plume but instead serves primarily to introduce a pressure difference between the top of the ramp surface and the gap between the adjacent injectors. The pressure is higher on the ramp surface, which creates a driving force for the flow to spill from the ramp surface into the gap between the adjacent injectors. This spillage introduces large counter rotating vortices on either side of the ramp injector body with the size and circulation proportional to the ramp height.[38] These vortices are large compared to the size of the fuel ports. Therefore, when they begin to interact with the injected fuel streams, they stretch and push the fuel-air interface upward away from the plate boundary layer and into the core of the flow. However, it should be noted that for the current ramp injector, the CVP is constrained by the narrow spacing between the adjacent injectors, which limits the size

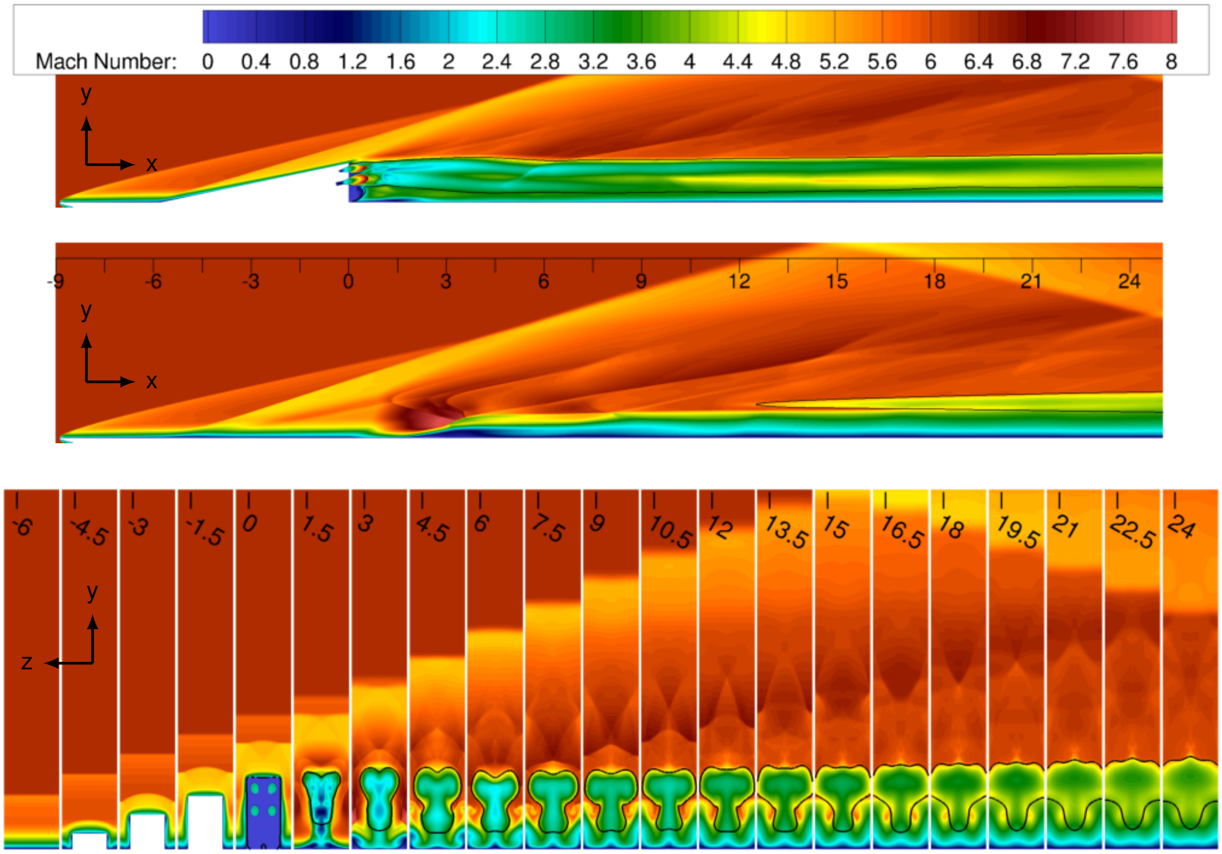

Figure 8. Contours of the Mach number on the streamwise planes obtained through the center of the injector ports, and half-way between the injectors, and cross-stream planes at various downstream locations for the ramp injector CFD simulations. Downstream distance is in inches. Black lines denote the stoichiometric value of the fuel mass fraction.

and strength of the CVP, and therefore, the upward movement of the fuel plume. This movement of the fuel into the core flow is, however, aided by the fact that all the ramp fuel ports are angled at 11.8 degrees up and the top set is angled at 10 degrees outward toward the gap between the adjacent injectors. Nevertheless, the combined effect of the angled injection and the large-scale CVP spreads the fuel through the intended fueling area. These effects can be seen by observing the stoichiometric value of the fuel mass fraction as it evolves in the cross-stream planes in Fig. 8.

For the flushwall injector, shown in Fig. 9, the flow features and dynamics are somewhat similar to that of the ramp injector. An oblique bow shock wave is generated by the fuel entering into the supersonic cross-stream. The oblique shock wave angle is about 16 degrees at the injector centerline. This bow shock interacts and joins with the same bow shock wave produced by the adjacent injector fuel plumes. Similar to the shock generated by the ramp body, the flushwall injector oblique shock wave does not significantly interact with the fuel-air mixing plume but instead serves primarily to introduce a pressure difference between the top of the fuel plume and the gap between the adjacent injectors. The pressure is higher on the top of the plume, which creates a driving force to form a CVP around the fuel plume. This CVP is too weak to significantly deform the stoichiometric isosurface, nevertheless it does provide an upward lifting motion as the fuel is convected downstream. A secondary CVP also forms inside the stoichiometric isocontour line. This CVP is driven by the underexpanded fuel plume penetrating into the supersonic crossflow and can be seen at the x = 3 station on Fig. 9. Because the flushwall injector is

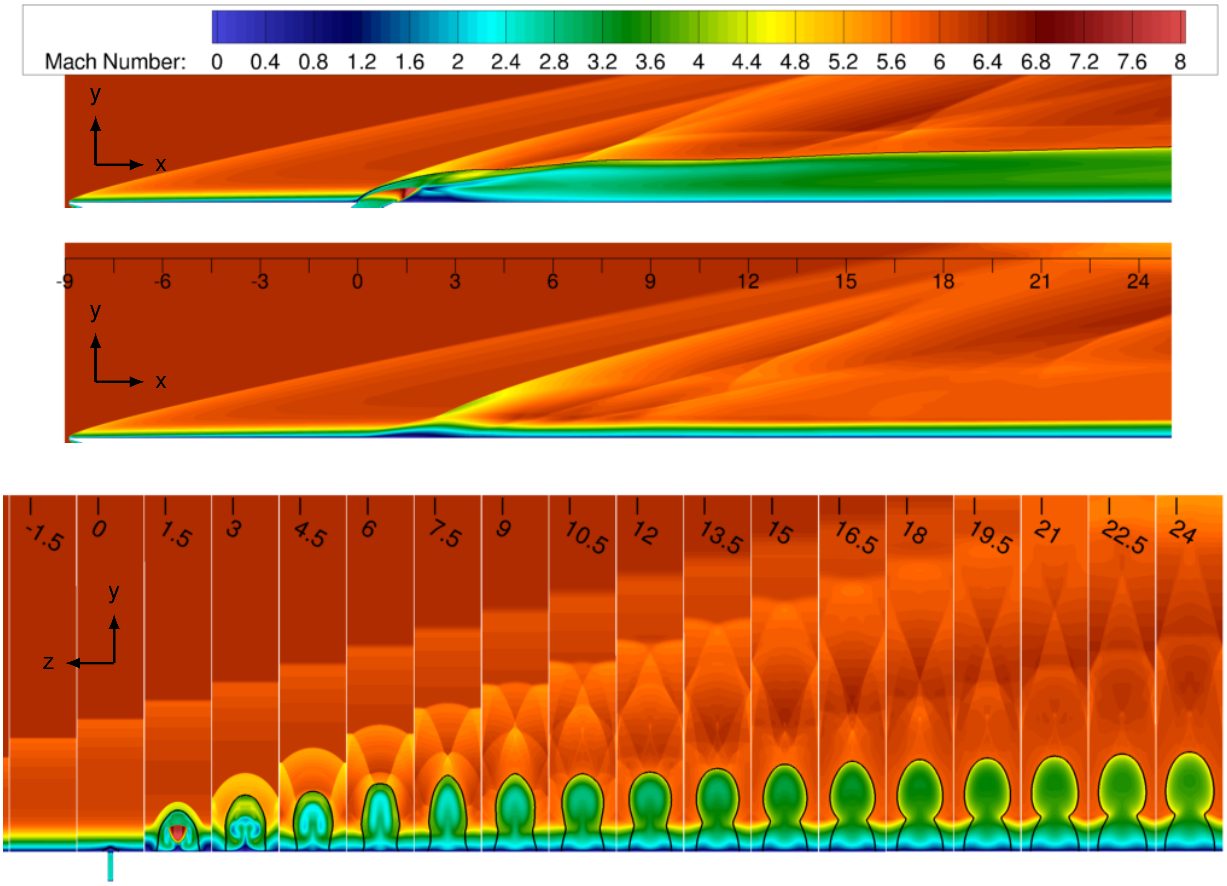

Figure 9. Contours of the Mach number on the streamwise planes obtained through the center of the injector port, and half-way between the injectors, and cross-stream planes at various downstream locations for the flushwall injector CFD simulations. Downstream distance is in inches. Black lines denote the stoichiometric value of the fuel mass fraction.

underexpanded (i.e., $p_f/p_a > 1$, see Table 1) the fuel plume spreads laterally in addition to penetrating into the crossflow. The underexpansion process redistributes some of the momentum (or dynamic pressure) of the fuel jet laterally, thereby reducing the amount available for penetration normal to the plate, and into the crossflow. Nevertheless, the penetration is comparable to that of the ramp injector.

Plots of the one-dimensional values of the mass-flux-weighted average mixing efficiency,[29] and total pressure recovery versus distance in inches are shown in Fig. 10 for the strut, ramp, and flushwall injectors. These plots help to quantify the overall behavior of the flow and the level of mixing and losses found among all of the simulated cases. The mixing efficiency indicates that the fuel and air mix the fastest for the strut injector, followed by the ramp, and the flushwall injectors. The profiles corresponding to the strut and ramp exhibit three distinct mixing regions, denoted on the figures. The first region, in the near-field of the injector body from 0 to about 2 inches (or about an injector body height), is characterized by a rapid rise in the mixing efficiency. The length of this region also correlates with the wake generated by the injector bodies. The fuel injected into this wake region has more time to mix with the surrounding air, thereby enhancing the mixing rate. This region is followed by a fairly long region where the mixing efficiency increases less rapidly and linearly with the downstream distance. The third region begins at about 22 inches and is characterized by a further decrease in the mixing rate. Unlike the strut and ramp injectors, the flushwall injector exhibits a much more linear increase in the mixing efficiency with the downstream distance. The total pressure recovery profiles are also shown in Fig. 10. Because the total pressure is proportional to the entropy, the

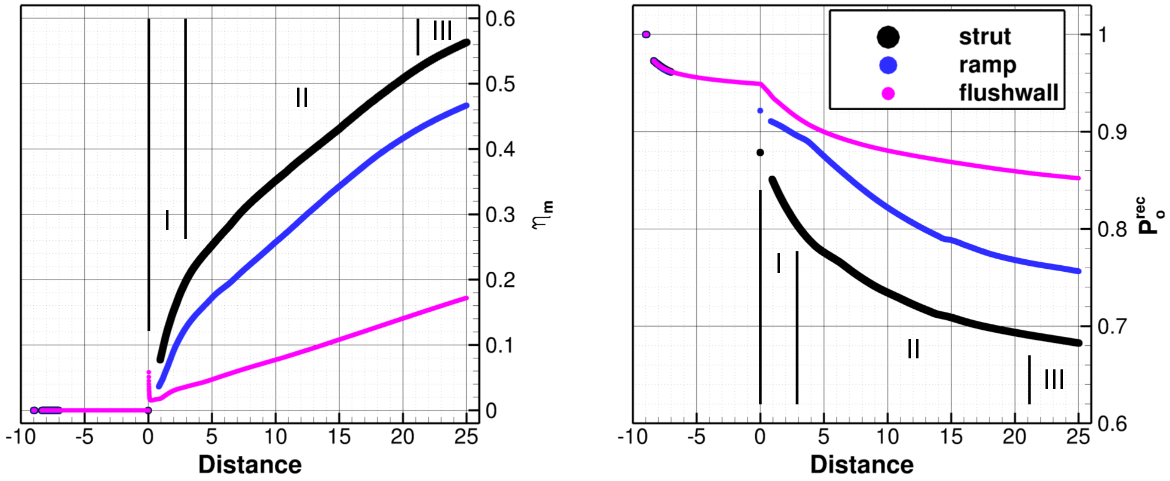

Figure 10. One-dimensional, mass-flux averaged, values of the mixing efficiency (left), and total pressure recovery (right) vs. the downstream distance (in inches). The vertical black lines and Roman numerals denote the three distinct mixing regions.

total pressure recovery can only decrease (in adiabatic flows). The decreases are due to shock and viscous losses upstream of the injection plane and also mixing downstream. For the strut and ramp injectors, about 8%–12% of the total pressure losses occur upstream of the injection plane with the strut body inducing almost twice as much losses as the ramp. This is not necessarily surprising because the current strut injector exposes almost twice as much surface area to the flow as the ramp injector, thereby inducing more viscous losses. In addition, the leading edge of the strut generates symmetric, cross-stream oblique shock waves, whereas, both the ramp and flushwall injectors only produce a single bow-like shock wave. Therefore, for the ramp and flushwall injectors, the shock losses are expected to be lower. Downstream of the injection plane, the mixing losses further contribute to the decrease. In general, the losses are proportional to mixing, i.e., greater mixing induces more total pressure losses. Therefore, although the flushwall injector exhibits significantly less mixing than either the strut or the ramp, it also exhibits the least amount of total pressure losses. This is a significant observation because the total pressure is proportional to the amount of momentum that can produce thrust.

SCHLIEREN

Prior to configuring the NO PLIF laser and optical hardware, a schlieren flow visualization system was set up and briefly used during tests of the strut injector to determine the efficacy of this technique to provide visualization of the fuel-air mixing. A z-type schlieren imaging system was used to visualize vertical density gradients through the fuel-air mixing region. A 20-W AmScope white LED illuminator fitted with a Thorlabs graduated ring-actuated iris diaphragm was used as the point source and was collimated by a 12-inch diameter, 60-inch focal length parabolic mirror. The resulting 12-inch diameter collimated light beam was aligned to run parallel to the z-axis (cross-stream) of the tunnel and flat plate surface. This collimated light was then refocused with a second 12-inch diameter, 60-inch focal length parabolic mirror on the opposite side of the tunnel. A horizontal knife edge was used to spatially filter the light at the point of focus and provide sensitivity to vertical density gradients in the test section. An Edmund Optics 1312 CCD USB camera operating at 70 Hz was used to acquire the schlieren images. A schematic of this z-type schlieren setup is shown in Fig. 11.

Schlieren images were collected for the strut injector mixing flowfields during a 70 second long experimental run sequence that included schlieren imaging before and during facility start-up as well as during the unfueled and fueled injector operation at ER of 0.5, 1.0, and 1.5. The resulting sequence of images consisted of about 4900 individual schlieren images. The initial image postprocessing step included removing the relative motion of the camera with respect to the tunnel from the individual images. This motion was caused by the mechanical vibration of the facility and resulted in small image-to-image translations, that impacted other postprocessing steps. ImageJ,[39] an open-source image processing program maintained by the National Institute of Health, was used with the Template Matching and Slice Alignment plugin[40] based on the OpenCV[41] library, to remove this apparent motion. The resulting position-synchronized sequence of images was then time-averaged over 5 second long intervals of interest. These intervals consisted of: an interval prior to the start of the facility air flow, an interval during the steady-state facility operation but for the unfueled injector condition, and three intervals corresponding to the different injector fueling levels. The time-averaged image for the interval prior to the start of the experimental run served as a background that was subtracted from the other time-averaged images to suppress certain image artifacts (such as scratches in the windows), thereby improving the quality of the schlieren visualization. This background subtraction process was not effective without first removing the image-to-image motion due to the facility vibrations. After subtracting the background image from the other time-averaged schlieren images, each new image was contrast stretched to enhance the schlieren features. Figure 12 shows a single image prior to and after performing these postprocessing steps. In these images, the experimental flat plate is located at the top of the image, with the positive plate normal direction pointing down (see Fig. 2), and the strut injector just to the left of the straight edge of the image near the top-left section. This straight edge does not correspond to the trailing edge of the strut injector, but instead is a result of partial blockage of the schlieren light path by one of the facility external support beams.

An equivalent synthetic schlieren image was also obtained from the available CFD data for the strut injector. To that end, Tecplot™360[42] was used to compute the density gradient in the direction consistent with the vertical direction of the experimental schlieren setup from the strut injector CFD simulations. Because the schlieren technique represents a line-of-sight-integrated measurement, which is in general difficult, computationally intensive, and time-consuming to obtain from numerical data on an arbitrary grid, Tecplot™360

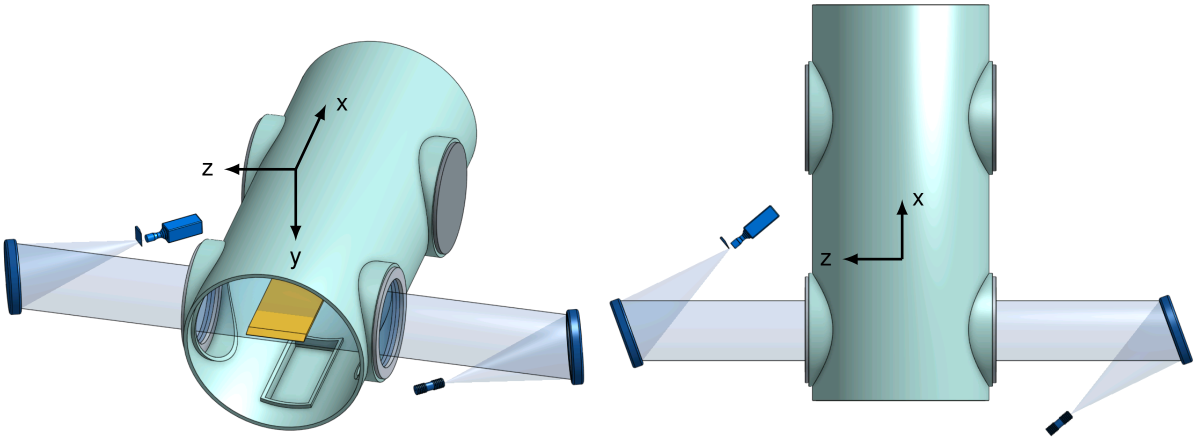

Figure 11. The isometric (left) and top (right) schematic views of the AHSTF facility test cabin with the front bulkhead removed exposing the experimental model and showing the z-type schlieren setup with the the light source, camera, knife edge, and mirrors positions (blue), as well as, the nominal light path. The facility air flow is from front-to-back or bottom-to-top.

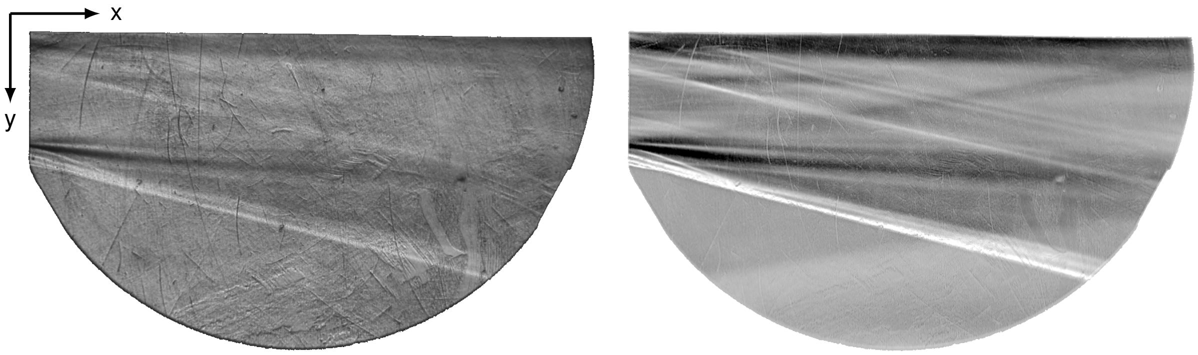

(a) Raw (b) Postprocessed

Figure 12. Raw and postprocessed time-averaged experimental schlieren images for the unfueled strut injector.

was used to extract a large number of streamwise planes from the simulation data. The total number of planes corresponded to about half the number of grid points in the direction along the line-of-sight of the schlieren. Tecplot^{TM}360 was then used to plot the contours of the relevant vertical density gradient on each plane, and a grayscale image, focusing on the same area as the experimental schlieren, was exported for each plane. This sequence of images was then imported into ImageJ, and the intensity of each pixel was pixel-by-pixel averaged for all of the planes using ImageJ Z-Project feature, resulting in a single image representing the line-of-sight average of the vertical density gradient. As a final step, and to ensure consistency with the experimental schlieren, the resulting line-of-sight average image was also contrast-stretched to enhance the visualization of the synthetic schlieren features.

NO PLIF

NO PLIF uses a UV laser sheet to interrogate a slice of the flow containing NO. This UV light excites fluorescence from the NO molecules, which is detected by a digital camera. One of NASA Langley's two mobile PLIF systems was installed next to the AHSTF facility as shown in Fig. 13. The two photos in Fig. 13 show the Mobile PLIF cart setup positioned to the left of the AHSTF facility, and the PLIF camera, collimating lens, and the translation stage installed on the AHSTF access door. The two schematics below the photos show the AHSTF test cabin with the facility nozzle and front bulkhead removed to reveal the experimental article, the laser path, and the camera, collimating lens, and the pedestal mirror positions during the streamwise and cross-stream diagnostic campaigns.

During the streamwise imaging, a horizontal laser sheet enters the test cabin and is reflected off a pedestal mirror located below the test article such that it illuminates the streamwise plane of the mixing region as shown in Fig. 13(c). Different streamwise planes are obtained by translating the laser sheet up and down, such that the camera-viewable streamwise plane translates toward and away from the fixed-position camera. The change in the viewing distance is perceived as a change in the PLIF image magnification and is corrected in postprocessing. During the cross-stream imaging, a vertical laser sheet is first collimated, then enters the test cabin and passes directly through the mixing region. To facilitate PLIF measurements of multiple downstream cross-stream planes, the laser optics and the camera are installed on a translation stage (see Fig. 13(b)), and move together in the streamwise direction. To allow for the laser sheet to pass straight into the test cabin, the camera is offset from its original position in the streamwise configuration,

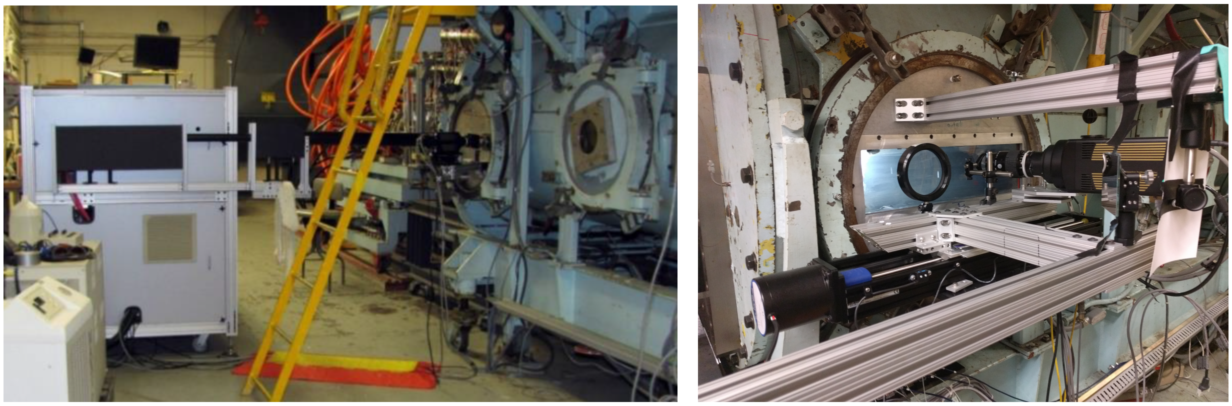

(a) Mobile PLIF cart (silver box on the left side of photo) next to the AHSTF (right)

(b) PLIF camera, collimating lens, and the translation stage installed on the AHSTF access door.

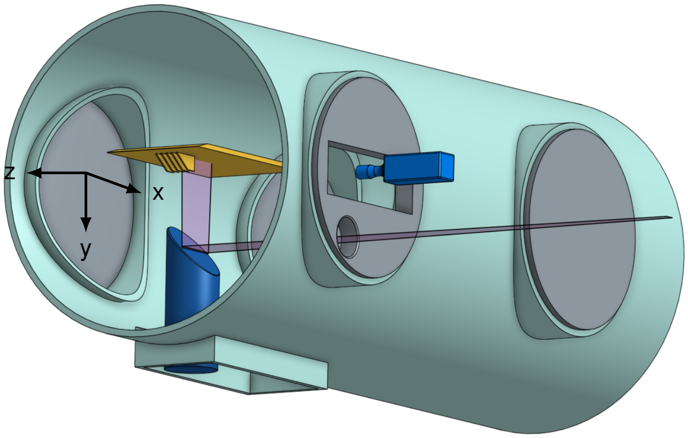

(c) Streamwise PLIF configuration

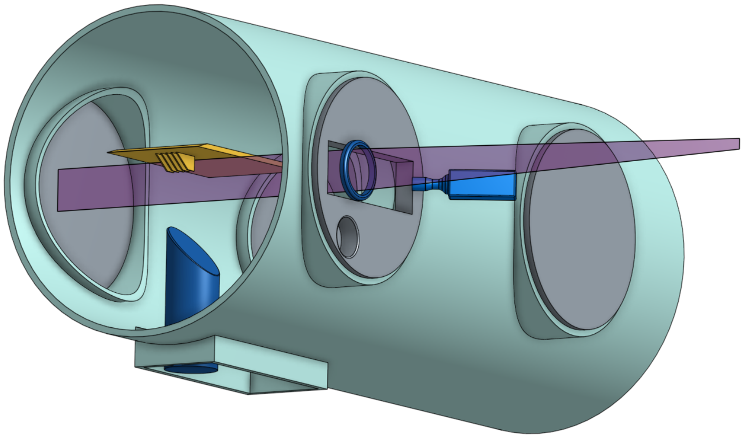

(d) Cross-stream PLIF configuration

Figure 13. Photos of the PLIF system installed in the AHSTF (a,b), and schematics of the streamwise (c) and cross-stream (d) PLIF configuration showing the path of the laser sheet (violet), and the camera, collimating lens, and the pedestal mirror positions (all in blue).

and rotated clockwise by about 17 degrees about the y-axis. Viewing the mixing region at such a relatively high angle of incidence to the laser sheet results in perspective-distorted PLIF images, which are corrected in postprocessing. Both the streamwise and cross-stream configurations were used for imaging for the strut injector. However, only the cross-stream configuration was used for the ramp and flushwall injectors.

The laser system uses a Spectra Physics Pro-230 Nd:YAG laser to pump a Sirah Cobra Stretch dye laser and Sirah Frequency Conversion Unit (FCU). The dye laser was operated near 624 nm and was sum-frequency mixed with the third harmonic of the Nd:YAG laser to produce the UV light used to excite NO. The resulting laser output, near 226 nm, was tuned to excite several weak spectral lines of NO to minimize absorption. The UV laser beam was formed into a laser sheet using a pair of lenses (usually a cylindrical lens followed by a spherical lens). This laser sheet then passed through the UV-grade fused silica glass facility windows into the test cabin and across the mixing region. High-efficiency filters (Layertec GmbH, Germany, <1% transmission at 226 nm and >80% transmission at 235-280 nm) were used to transmit the LIF signal while rejecting the laser scatter. The same cameras, excitation schemes, etc., were used in previous experiments.[18,20] The fluorescence was imaged onto a gated, intensified charge-coupled device (CCD) (Princeton Instruments PIMAX-II ®), and represented using 16-bits of resolution. A single Nikon ® UV lens with a focal length of 105 mm and f/4.5 aperture was used. The camera magnifications were measured by imaging a regular pattern of dots of known spacing (known as a dotcard), with the dotcard placed in the image plane. The images were obtained at a rate of 10 Hz with flow-stopping time resolution of about 100 nanoseconds. The final images were also postprocessed as discussed in the next section. The spatial distribution of the laser sheet intensity was not monitored, but could be inferred from uniform flow regions obtained in the images.

Three different sets of LIF transition lines are used in the current work. In terms of Hund's Case A notation[43] these are: $^{\mathrm{S}}\mathrm{R}_{21}(9.5) + \mathrm{Q}_1(20.5) +^{\mathrm{Q}} \mathrm{P}_{21}(20.5) + \mathrm{R}_2(18.5)$, $^{\mathrm{O}}\mathrm{P}_{12}(6.5) +^{\mathrm{O}} \mathrm{P}_{12}(14.5)$, and $^{\mathrm{R}}\mathrm{Q}_{21}(12.5) + \mathrm{R}_1(12.5)$, where the number in the parenthesis denotes the rotational quantum number. Figure 14 shows the spectral intensity of various LIF transition lines versus wavelength and wavenumber obtained from LIFBASE[44] simulations. The specific NO transitions probed are denoted on the individual figures. The profiles are plotted for the temperatures of 100 and 300 K and include Doppler and pressure (collision) broadening effects. These temperatures are representative of those observed in the PLIF experiments. The spectral intensity is also plotted for the temperature of 400 K but without the broadening effects (denoted as NB) to identify the wavelength of the specific transition lines. The thick black line denotes the laser spectral profile, which is assumed to be Gaussian. The laser linewidth, described by the full width at half maximum (FWHM), is about $2\,\mathrm{cm}^{-1}$ for the first set of lines, and $0.2\,\mathrm{cm}^{-1}$ for the latter two. It should be noted that although the FWHM of the laser profile is the same for Fig. 14(b,c), the extent of the wavelength axis in (c) has been reduced to show the double transition lines present in the latter. As a result, the laser profile appears broader in Fig. 14(c).

Each set of transition lines exhibits different sensitivity to pressure, temperature, and mole fraction of NO, and has different absorption characteristics. The $^{\mathrm{O}}\mathrm{P}_{12}(6.5) +^{\mathrm{O}} \mathrm{P}_{12}(14.5)$, and $^{\mathrm{R}}\mathrm{Q}_{21}(12.5) + \mathrm{R}_1(12.5)$, transition lines have been selected for their linear correlation with either mass fraction or mole fraction of helium, respectively. That is, the LIF signal corresponding to these two sets of lines correlated close to linearly with mass or mole fraction of helium in *a priori* analysis using LIF modeling software LINUS,[43] under the nominal pressure, temperature, and NO concentration conditions representative of those found in the current experiments. In addition, because, in the current experiments, the NO is present in the facility air and the fuel simulant is "unseeded" (contains no NO), the dark, no-signal regions, are representative of the fuel stream, and conversely, bright regions contain air. This approach, although convenient from an experimentation point of view because NO is naturally produced in the facility arc-heater, makes the LIF more susceptible to the attenuation of signal due to absorption because the laser light has to pass through about 2 feet of the test cabin filled with NO-containing air en-route to the PLIF imaging region. A priori estimates of absorption through the test cabin using LINUS under expected tunnel operating conditions suggest that up to 75% laser energy could be absorbed before reaching the field of view of the CCD camera.

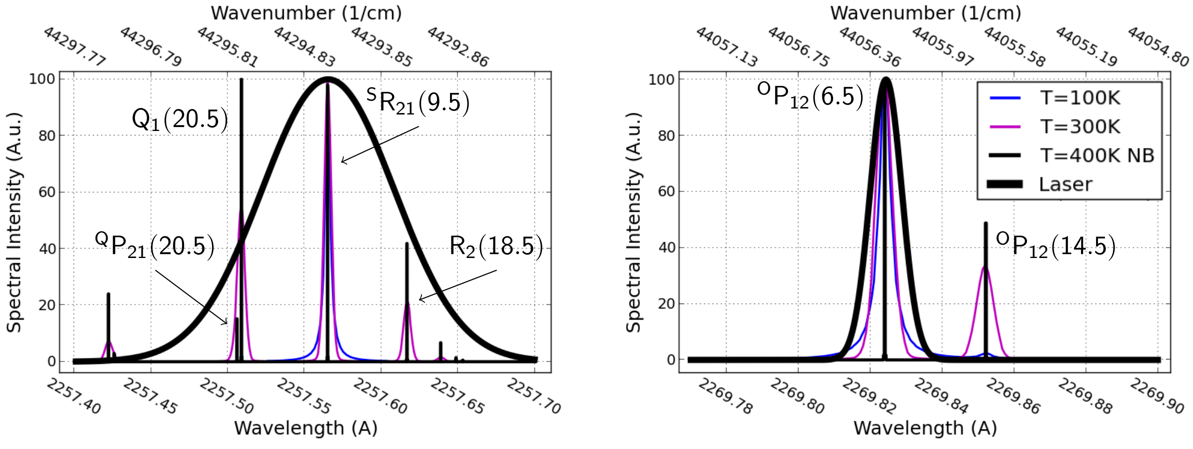

(a) Transitions probed for the streamwise PLIF. FWHM of laser is about 2/cm

(b) Transitions probed for the mass-fraction-sensitive PLIF. FWHM of laser is about 0.2/cm

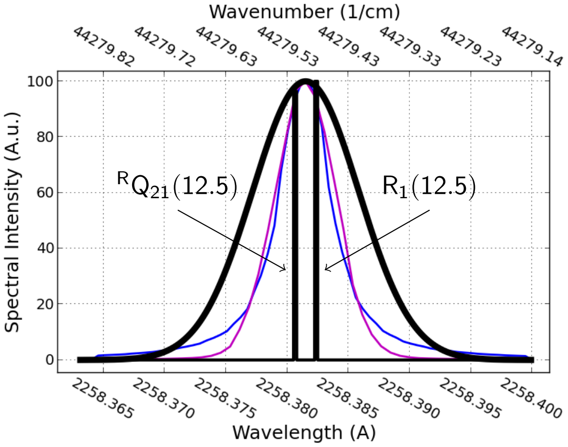

(c) Transitions probed for the mole-fraction-sensitive PLIF. FWHM of laser is about 0.2/cm

Figure 14. Spectral intensity of various NO transition lines considered in the current experiments vs. the wavelength (or wavenumber) for several temperatures of air in vacuum. The lines plotted for the temperatures of 100 and 300 K include Doppler and collisional broadening effects, whereas the line plotted for the temperature of 400 K, denoted by NB (no broadening), does not, in order to pinpoint the wavelength of the specific transition. The thick black line denotes the laser spectral profile, assumed to be Gaussian. The specific NO transitions probed are also denoted on the figure using Hund's Case A notation with the rotational quantum number in parenthesis. Spectral intensity data for the NO transitions was obtained from LIFBASE.[44]

PLIF IMAGE POSTPROCESSING

The instantaneous, raw PLIF images typically require some amount of postprocessing. The corrections can include manipulations that do not alter the raw value of the PLIF signal, such as image magnification adjustments, and/or perspective control (unwarping), and those that alter the value of the PLIF signal, such as adjustments to the signal "zero" reference, corrections for laser sheet and shot-to-shot intensity variations, and image-intensity-based corrections for laser sheet absorption. The final postprocessing step may also include time averaging to allow for comparisons with time-averaged simulation data. In the current work, ImageJ software is used for all image postprocessing and analyses. An example of a few of the steps are shown in Figs. 15–18.

Figure 15 shows the raw and unwarped cross-stream PLIF images along with the raw and target dotcards used in the perspective correction process of the mixing flowfield 0.5 inches downstream of the strut injector. The perspective correction or image "unwarping" step is required when the resulting image is distorted either by the optics and/or the viewing angle. In the current experiments, this postprocessing step is applied to both streamwise and cross-stream PLIF images. The former images require relatively minor corrections of the distortions introduced primarily by the optical elements (lenses, windows, etc.) of the PLIF setup. The latter images are corrected for perspective distortions (see Fig. 15(a)) introduced by viewing the laser sheet at the relatively high angle of incidence of about 73 degrees. The unwarping effectively involves computing a transformation function that maps and interpolates the pixels from the dotcard imaged at the laser sheet location (Fig. 15(b)) to the target dotcard viewed at a zero angle of incidence (Fig. 15(c)). This transformation function is then applied to all of the raw PLIF images (e.g., Fig. 15(a)) to obtain the corresponding unwarped images (Fig. 15(d)). All of the raw PLIF images are obtained with a 512 x 512 pixel resolution. The resolution of the unwarped images is set such that the highest pixel density (in pixels per inch) in the raw image is used for the entire unwarped image. For example, the highest pixel density in the raw PLIF image in Fig. 15(a) can be obtained by counting the rows of dots along the left-most edge (nearest to the camera) of this image and dividing by the known distance between those rows. With the distance between the dots on the dotcard at 0.25 inches, the approximate maximum pixel density of the raw PLIF image is 146 pixels per inch. Therefore, the resolution of the 9.6 x 3.75 inch target dotcard (Fig. 15(c)) used for unwarping is set to 1409 x 550 pixels. The inverse of the pixel density is the spatial resolution of the image, which is about 6.9 thousandths of an inch (0.175 mm) per pixel. Coincidentally, this is nearly identical to the spatial resolution used for the RAS on the fine grid in the same region, which was 7 thousandths of an inch (0.179 mm) per grid size. Under the current flow conditions (see Table 1), this level of spatial resolution is sufficient to effectively freeze the flow features along the fastest streamwise direction using a 100 nanosecond laser pulse. That is, a fluid particle traveling along the streamwise direction at a nominal free-stream velocity will travel a distance equal to less than a single pixel during each 100 nanosecond laser pulse. This feature of the PLIF system is important because it eliminates laser pulse time-averaging of the spatial flow features resolved in the images. Nevertheless, it should be noted that this does not mean that all flow features are resolved. On the contrary, any turbulence fluctuations that are subpixel scale, and sub-laser pulse time scale are effectively averaged (potentially in a nonlinear manner) by the PLIF system. The amount of physical "information" that is averaged (either spatially or temporally) depends on the local Reynolds number of the flow, and the corresponding Kolmogorov length and time scales.[45,46]

Figure 16 shows the unwarped but otherwise yet uncorrected PLIF image of the same strut injector, and the corresponding image corrected for left-to-right laser sheet absorption. Plots of the PLIF intensities for the raw and corrected images versus distance in pixels measured in the direction of the laser sheet absorption along the bottom few pixels of each image (i.e., away from the mixing regions) are shown to the right of the images. The raw image exhibits about a factor of two to four attenuation of the PLIF signal as the laser light is absorbed by the NO molecules. The image intensity-based correction procedure involves sampling the image intensity from an area away from the mixing region where the intensity is expected to vary. For the cross-stream images, this area is denoted by the small box in Fig. 16(a). The new image intensity is obtained by dividing every pixel in the image by its sampled cross-stream value of the intensity from the box. This procedure can only partially correct for the laser light absorption effect because the nominal absorption intensity is based on localized left-to-right intensity variation, although in the current image the correction is quite effective. However, it should also be noted that the signal-to-noise ratio decreases from left-to-right as a result. The hills and valleys visible in the line plots are a result of the expected sensitivity of the PLIF signal to both pressure and temperature, and no attempt is made to correct for these variations.

Figure 17 shows a streamwise PLIF image before and after full postprocessing, and the line plots of the mean value of the PLIF signal intensity computed from the central lower half portion, denoted by a box, of every image versus the image number. These plots indicate that before postprocessing the shot-to-shot PLIF signal intensity can vary by as much as a factor of two. These variations are due to both the streamwise

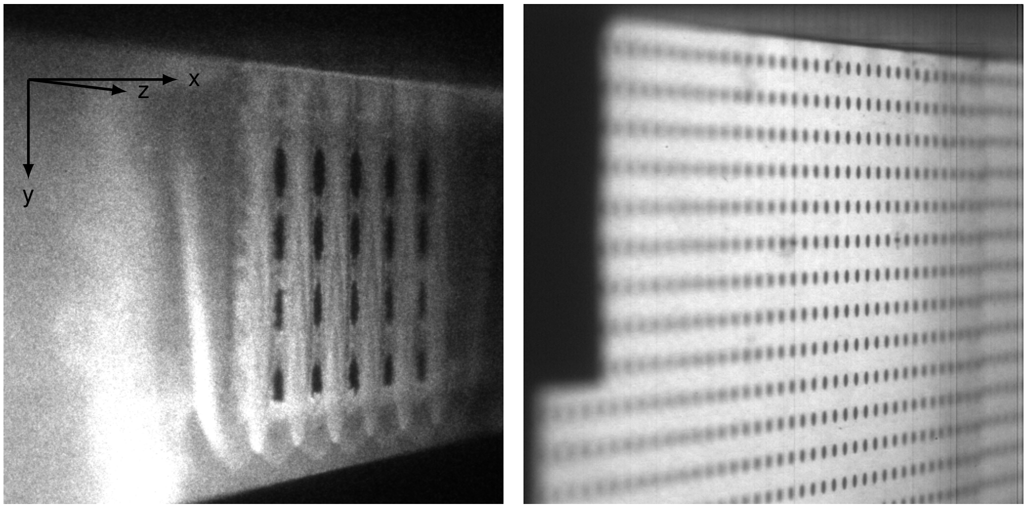

(a) Unaltered, raw, cross-stream PLIF image of the mixing flowfield downstream of a strut injector.

(b) Dotcard image taken at the location of the laser sheet.

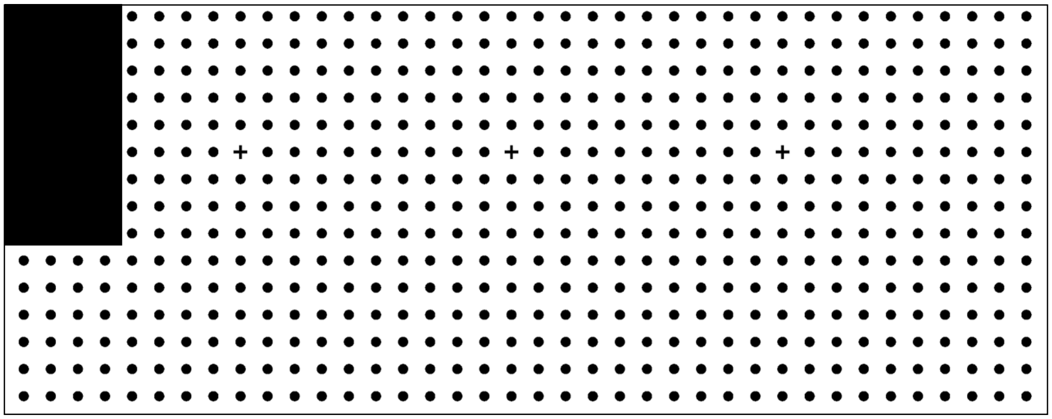

(c) Undistorted target dotcard used for the image in (b).

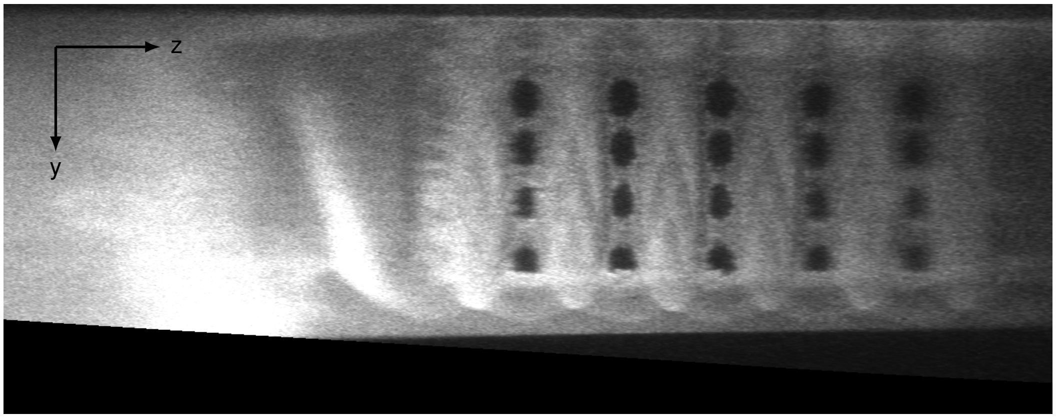

(d) Corrected (or unwarped) image corresponding to (a).

Figure 15. Raw PLIF image, distorted and undistorted dotcards, and the corresponding corrected (unwarped) PLIF image at 0.5 inches downstream of a strut injector.

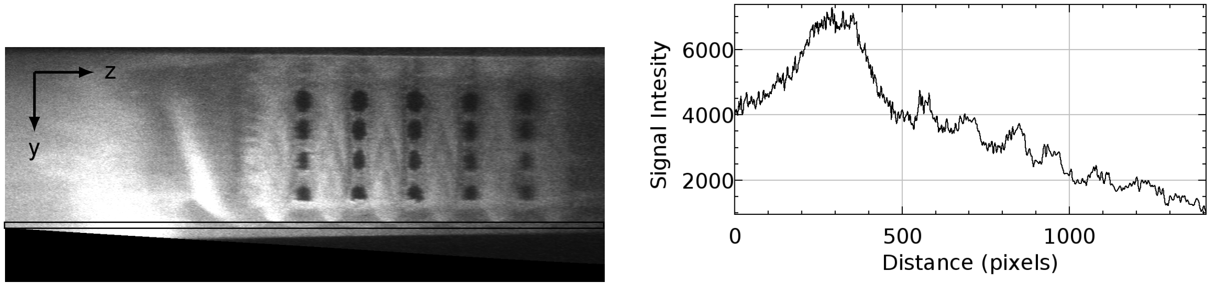

(a) Unwarped, raw PLIF image. Box denotes area sampled to estimate left-to-right laser light absorption.

(b) Raw PLIF signal from the boxed area in (a)

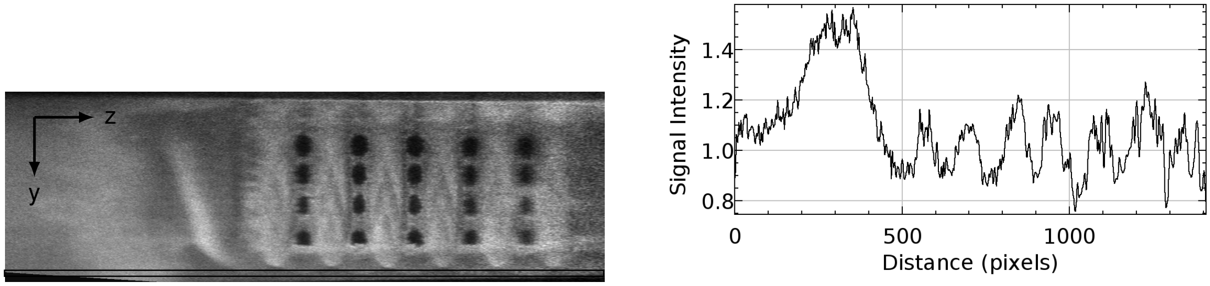

(c) Unwarped, postprocessed PLIF image. Box denotes area sampled to verify left-to-right laser light absorption correction.

(d) Postprocessed PLIF signal from the boxed area in (c)

Figure 16. Unwarped raw and postprocessed cross-stream images of the mixing flowfield downstream of the strut injector and corresponding PLIF signal vs. left-to-right image pixel count.

laser sheet intensity variations as well as the time-varying amount of NO produced by the facility. To correct for the former, a variation of the correction used for laser light absorption, and discussed above, is applied. The latter is corrected by dividing each pixel in an image by the mean value of the signal intensity computed from the boxed area. The applied corrections significantly reduce the shot-to-shot variations allowing for construction of more equally weighted averages for comparisons with time-averaged simulation data. The slight spike in the mean image intensity values occurring for corrected images ranging from about 420 to 460 is due to the loss of signal to a portion of the image due to the motion of the laser sheet that gets amplified in a correction process. Similar loss of signal occurs for the last one hundred images that were collected during the shutdown sequence of the experimental facility. These images were not used in averaging of the streamwise PLIF data.

Finally, Fig. 18 shows the time-average of 30 frames (3.0 sec.) of the postprocessed cross-stream PLIF images. All corrections discussed above have been applied to the individual image frames before averaging. Notable in the image is the increasing level of blurriness when moving away from the central strut injector. This loss of focus is a result of imaging at a relatively high angle of incidence to the laser sheet and can also be observed in the dotcard image of Fig. 15(b). Although the perspective can be corrected, the loss of focus cannot. However, in future experiments, the Scheimpflug principle can be adopted to improve the focusing when performing cross-stream PLIF imaging at high angle of incidence.

The run-to-run variability in the PLIF imaging can be visually examined in Fig. 19. The rows (from top to bottom) show time-averaged cross-stream images obtained at several downstream locations from the ramp injector face, while the left and right columns show the data obtained from two successive runs. These images were obtained by tuning the laser to mass-fraction-sensitive LIF lines. The first two rows show fuel-off and -on conditions, respectively, at 0.5 inches downstream of the injector face, followed by fuel-

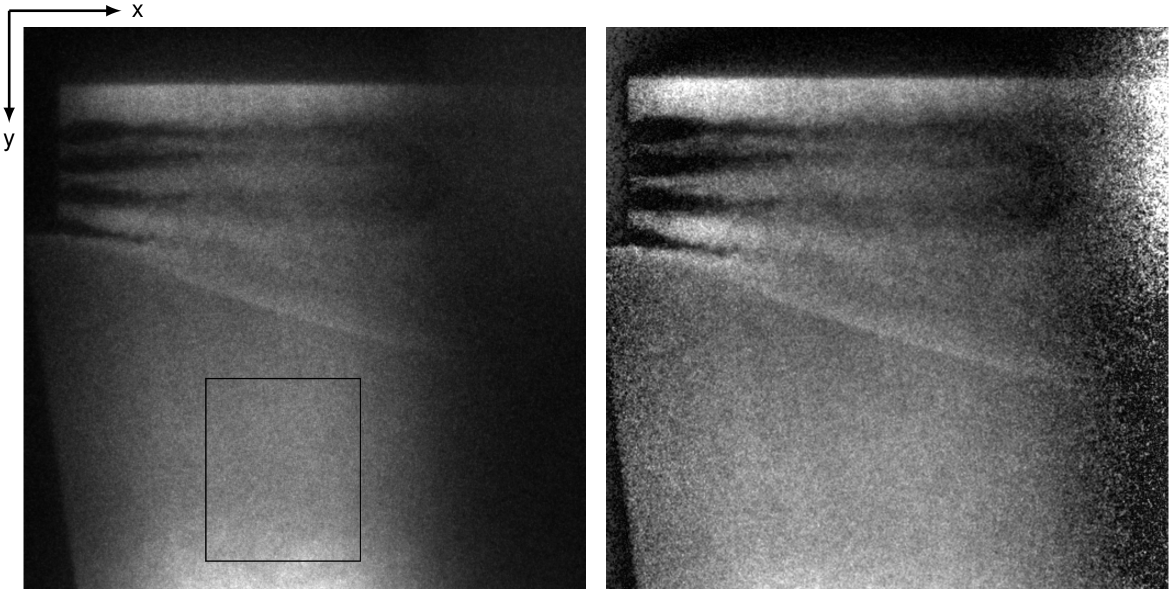

(a) Raw PLIF image. Box denotes area sampled to measure shot-to-shot intensity variation.

(b) Postprocessed PLIF image

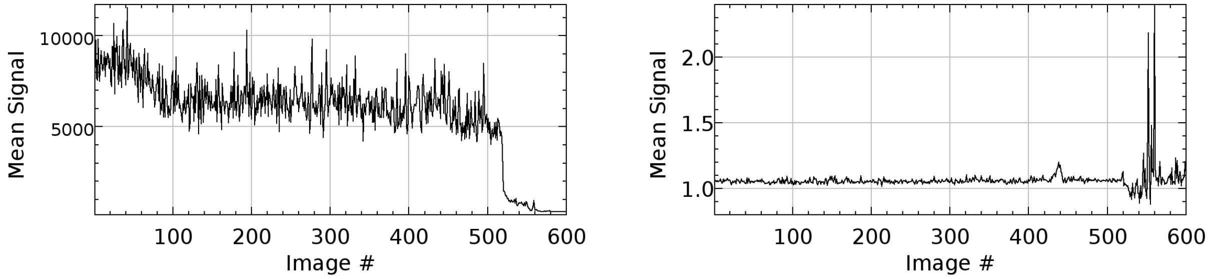

(c) Mean signal intensity vs. image number for the raw PLIF images sampled from the boxed area in (a).

(d) Mean signal intensity vs. image number for the postprocessed PLIF images sampled from the same boxed area as in (a) but from (b).

Figure 17. Raw and postprocessed streamwise PLIF images of the strut injector and the corresponding mean PLIF signal vs. image number.

on imaging at 1.0, 2.0, and 4.0 inches downstream. Although the images from different runs are nearly indistinguishable, notable in the imaging is a band of strong absorption that could not be corrected by the current image postprocessing approach.

Figure 20 also shows run-to-run variability in the PLIF imaging, however, this time the data sets were obtained about eight months apart. The downstream locations are the same as those above, however, these data were obtained using the mole fraction, instead of mass fraction, sensitive LIF lines. As those in Fig. 19, these images are qualitatively similar indicating robustness and good repeatability characteristics of both the facility and the current PLIF approach.

Given the relative success in applying image postprocessing corrections to the PLIF data, and the good quality of the PLIF time-averaged images (e.g., Fig. 18), a three dimensional (3D) image reconstruction technique, similar to that used in magnetic resonance imaging (MRI) was also performed in the present work. The motivation for performing the 3D reconstruction is to investigate the fidelity of the flow visualizations on the reconstructed image planes. A satisfactory outcome would eliminate the need to reconfigure

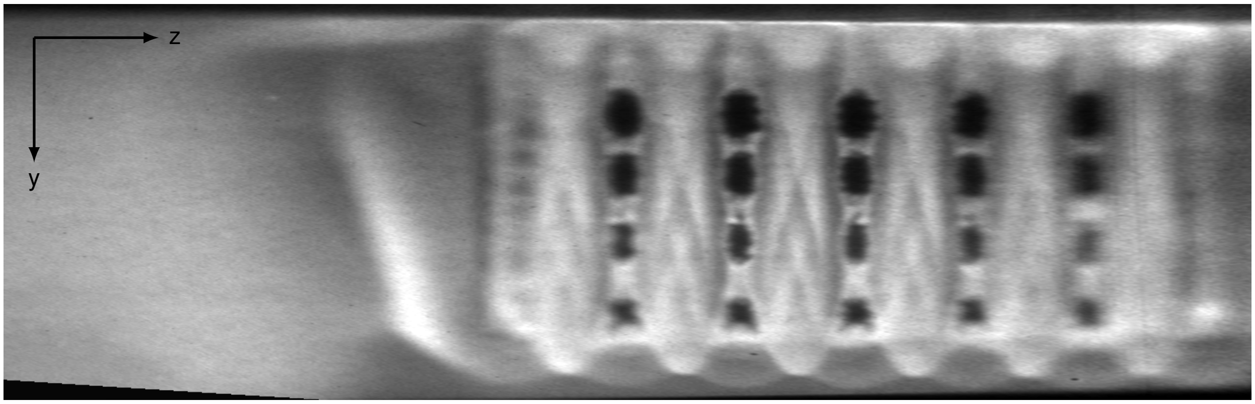

Figure 18. Time average of 30 frames (3.0 seconds) of the postprocessed cross-stream images for the strut injector at x=0.5 inches.

the PLIF optical setup for each orthogonal plane of interest, and instead allow for a single PLIF setup to be used to investigate the entire 3D mixing flowfield. In the current work, the cross-stream PLIF imaging is used for the reconstruction. The reconstruction approach relies on steady flow conditions and a slow and continuous translation of the collimated laser sheet while collecting the PLIF data. Figure 21 shows a plot of the laser sheet position and the ER versus time during a typical experimental run in the cross-stream PLIF configuration. The translation stage is calibrated such that the zero position corresponds to the trailing edge of each fuel injector. The laser sheet translation stage travel rate is obtained by computing the average value of the slope of the laser position during the translation interval. The distinctive stair-stepping in the plot of the laser position corresponds to the dwell locations where the collected PLIF images can be time-averaged. The 3D reconstruction data are obtained during the translation phase from the time of about 25 to 38 seconds in the figure. The laser sheet was initially positioned just downstream of the injector trailing edge. It was then first moved upstream until the injector hardware trailing edge obstructed the laser sheet, and then back downstream at a steady rate of translation (e.g., see time range of 22-to-25 seconds in Fig. 21). This step allowed for visual identification and verification of the position of the trailing edge of the injector during each experimental run, and computation of any positional offset corrections as needed.

Unlike the data obtained at the dwell points, the PLIF images obtained during translation represent instantaneous realizations at different positions and cannot be time-averaged. However, all of the other image postprocessing steps discussed above, i.e., unwarping, image intensity corrections due to laser profile variations and absorption, and shot-to-shot intensity variation corrections, are applied to each image prior to performing the 3D reconstruction procedure. It should be noted, however, that each instantaneous PLIF image does represent a partial average over the flow-stopping resolution of the PLIF setup, which, for the current experiments, is estimated to be about 100 nanoseconds. With this caveat, and noting that the consecutive PLIF frames are obtained every 100 microseconds (i.e., at a rate of 10Hz), which is larger than the time-scales associated with the turbulence at Reynolds numbers found in the current experiments, the consecutive PLIF images are expected to be statistically independent in addition to being spatially distinct. Although, statistically independent images are desired (or even required) for obtaining accurate time-averages in a turbulent flow, these images do represent independent realizations of a chaotic turbulent flow, and combining such images into a 3D reconstructed field is similar to performing an MRI of a rapidly vibrating object. That is, some smearing, blurring, and random “shifting” of flow information in the reconstructed image is to be expected as a consequence of turbulent motions.

The 3D reconstruction approach in the current work was only applied to the cross-stream PLIF data. The streamwise dimension was reconstructed from the cross-stream PLIF images by using the Orthogonal Views feature of ImageJ. This feature automatically extracts a user-defined line of pixels from a sequence of images and assembles the extracted lines into a single new image from left-to-right in the order in which

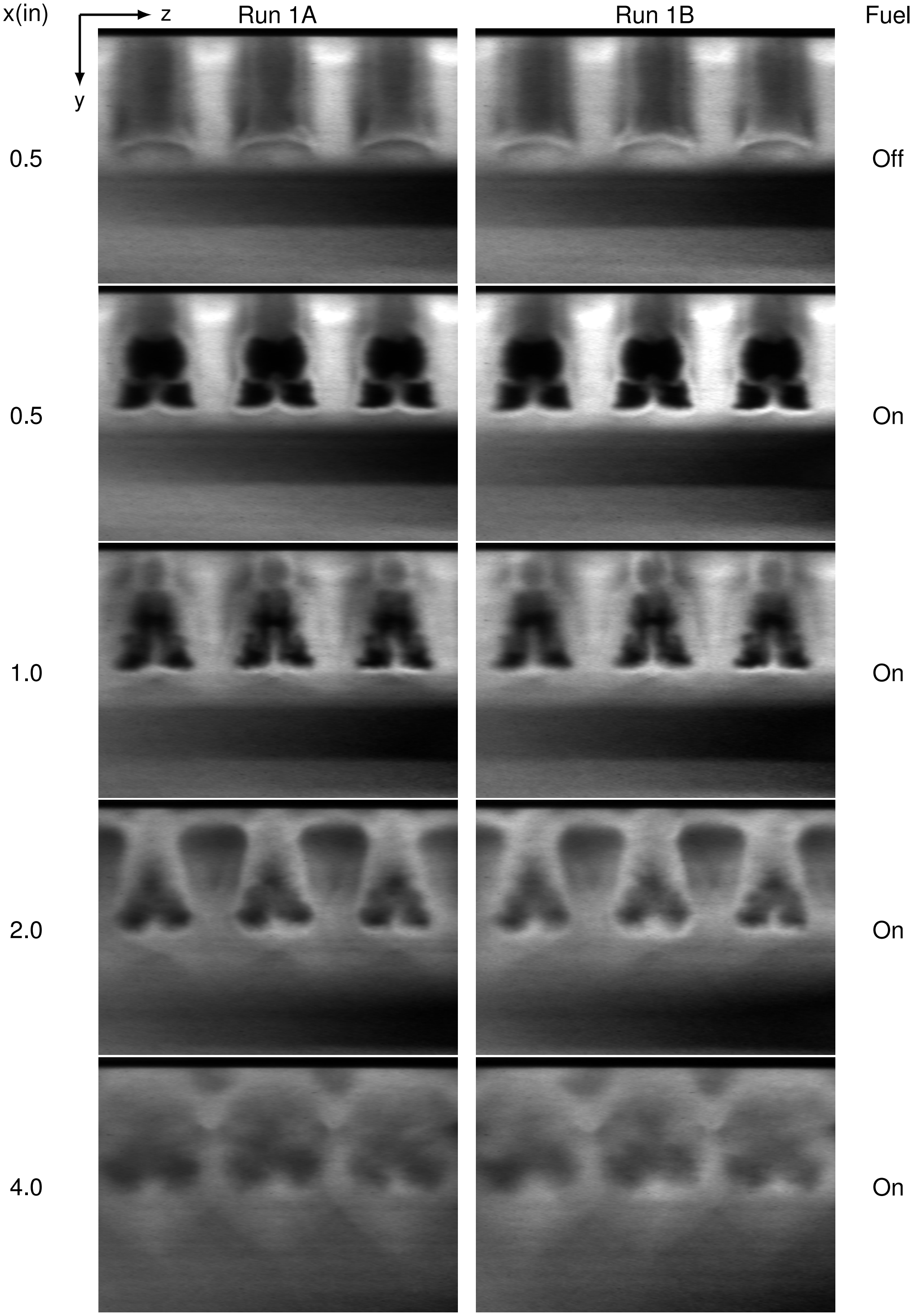
x(in)
z
y
Run 1A
Run 1B
Fuel
0.5
Off
0.5
On
1.0
On
2.0
On
4.0
On

Figure 19. Time-averaged cross-stream PLIF images for the ramp injector for two different consecutive experimental runs at the same nominal conditions and obtained using mass fraction sensitive LIF lines. The images are located at (from top to bottom): 0.5, 1.0, 2.0, 4.0 inches downstream of the injector face, with the first two rows showing fuel off and on condition, respectively, at 0.5 inches.

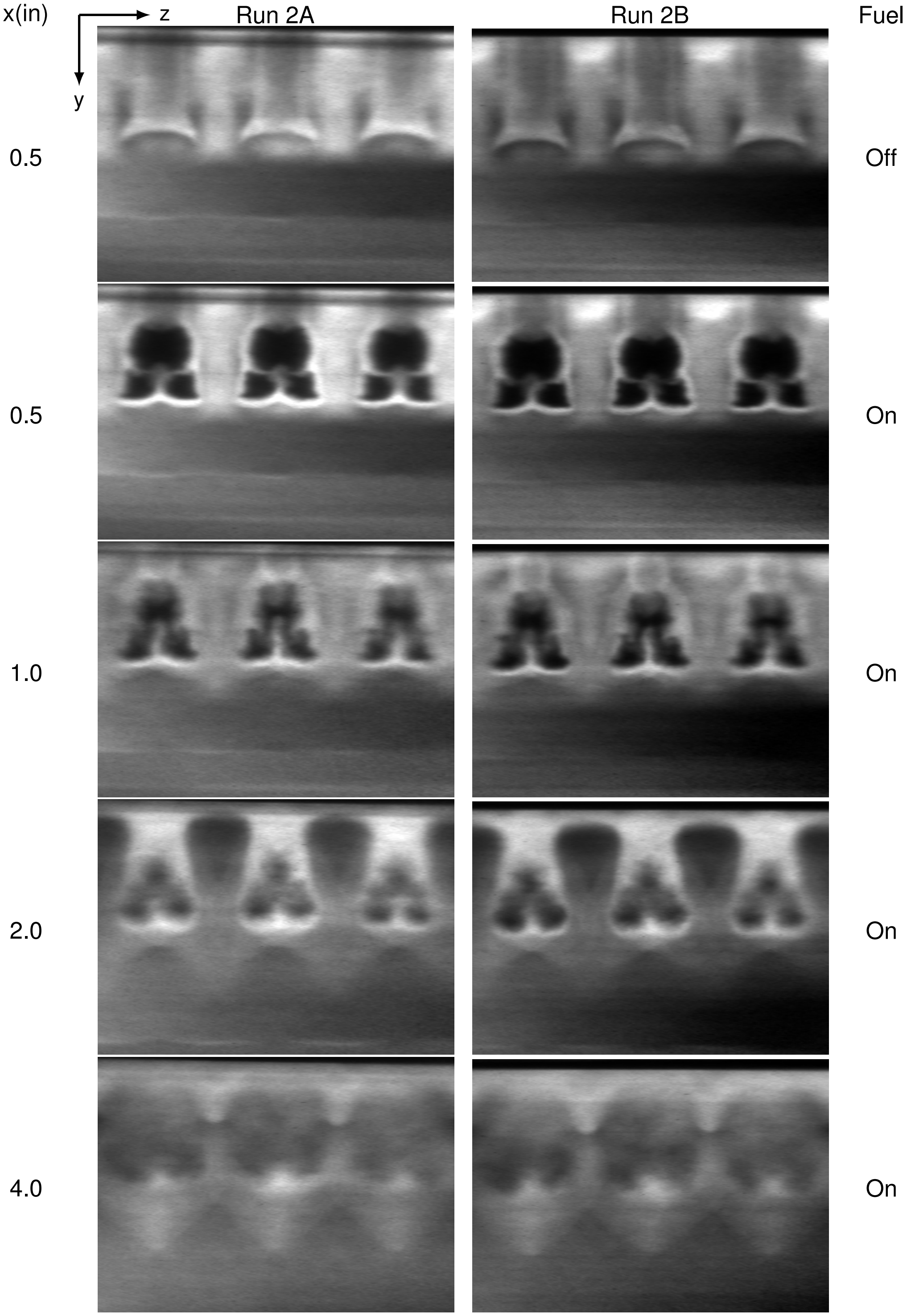
x(in)
z
y
Run 2A
Run 2B
Fuel
0.5
Off
0.5
On
1.0
On
2.0
On
4.0
On

Figure 20. Time-averaged cross-stream PLIF images for the ramp injector for two different experimental runs performed about eight months apart at the same nominal conditions and obtained using mole-fraction-sensitive LIF lines. The images are located at (from top to bottom): 0.5, 1.0, 2.0, 4.0 inches downstream of the injector face, with the first two rows showing fuel off and on condition, respectively, at 0.5 inches.

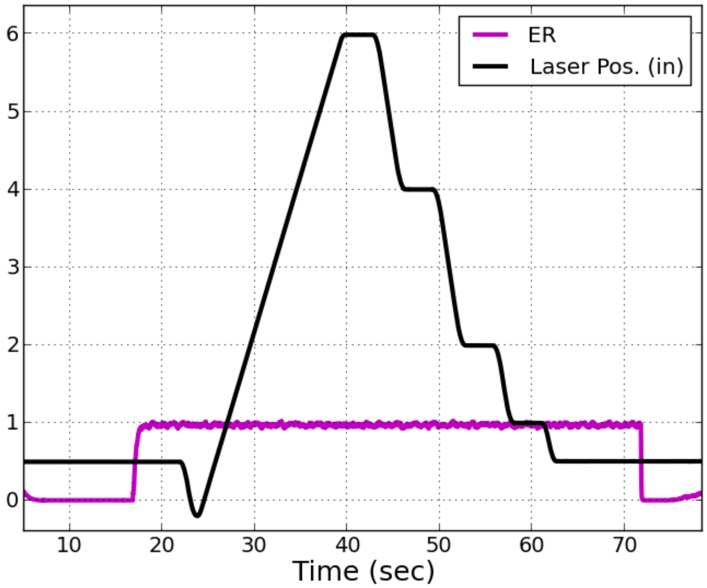

Figure 21. Representative plot of the laser translation stage streamwise position, in inches downstream of the injector exit plane, and the ER vs. time during a typical experimental run.

they were extracted. The line of pixels can be either horizontal or vertical with respect to the source image. The streamwise resolution of the resulting image is equal to the the total number of images in the source sequence used for the reconstruction. The resolution of the other dimension is unchanged from that of the source image. Because the number of images in the image sequence can be arbitrary, a rescaling procedure must be applied to the streamwise resolution. This rescaling is computed in such a way as to ensure that the number of pixels per inch is equal along both image dimensions. To achieve this, the scaling ratio for the new streamwise dimension can be obtained from:

$$SF(pixels/frame) = \frac{STR\,(in/s)}{FR\,(frame/s)} \times TDR\,(pixels/in), \tag{1}$$

where SF, STR, FR, and TDR are the streamwise dimension scale factor, laser sheet translation stage travel rate, PLIF frame rate, and target dotcard image resolution per inch, respectively. The quantity SF corresponds to the number of pixels that each extracted pixel line represents in a new image. When this number is greater than one, the rescaling process involves interpolation that blends adjacent lines to complete the image. Because the laser sheet translation stage travel rate is set experimentally, a special case of Eq. 1 is when $SF = 1$, which gives

$$STR = \frac{FR}{TDR}. \tag{2}$$

Under this condition, the image streamwise dimension rescaling step can be omitted from the 3D reconstruction procedure because each extracted pixel line represents exactly one pixel in the reconstructed image.

FLUORESCENCE MODELING

The PLIF signal level S (number of counts recorded on a pixel of the detector) is a function of temperature, pressure, mole-fraction, flow velocity, and a number of known experimental parameters. A model for the fluorescence signal in the weak fluorescence regime is given by Paul et al.:[47]

$$S \propto \frac{\chi_{NO}}{k_B T}\, \phi(P,T,\chi_\alpha) \sum_i \left(f_B(T,J)\, B_{12}(J)\, g(v_0, v_l, \Delta v_l, P, T, \chi_\alpha, u_\parallel) \right)_i , \tag{3}$$

where χ_{NO}, χ_α, P, T, k_B, f_B, J, B_{12}, g, v_0, v_l, Δv_l, and $u_\parallel$ are the mole fraction of NO and species α in the mixture, mixture pressure and temperature, Boltzmann constant, Boltzmann fraction, rotational quantum number, Einstein absorption coefficient, spectral overlap integral, transition line center absorption wavenumber, laser center wavenumber and FWHM, and velocity parallel to the laser sheet, respectively. The ratio ϕ, defined as

$$\phi = \frac{A_{21}}{A_{21} + Q(P,T,\chi_\alpha)}, \tag{4}$$

is the fluorescence yield, where A_{21} and Q are the Einstein spontaneous emission rate and quenching rate, respectively. The summation in Eq. 3 is over all transition lines i, which are excited by the laser. The proportionality in Eq. 3 can be removed by introducing a constant that describes the optical system. In addition, Eq. 3 contains nonlinear dependencies on pressure, temperature, and mole fraction of species in the mixture through the Boltzmann fraction, the spectral overlap integral, and the quenching rate. Furthermore, the spectral overlap integral also accounts for signal attenuation due to any laser "detuning" from the intended transition line, and the Doppler effect. All quantities are modeled following the assumptions and the approach of Paul et al.,[47] and Ivey et al.[20] with the model constants and coefficients obtained from LINUS. Additional PLIF modeling details are also available in the appendix.

The above model was applied to the CFD data to obtain CFIs equivalent to those obtained experimentally with PLIF. However, it should be noted that, due to the strong nonlinearities in the model, applying it to the RAS data, which represents time-averages, is expected to introduce some errors. This is in contrast to the experimentally obtained PLIF images, which are instantaneous and time-averaged in the post-processing step. Consequently, the LIF signal obtained from RAS is only an approximation of the experimental PLIF, i.e.,

$$S_{RAS}(\overline{P}, \overline{T}, \overline{\chi_\alpha}, \overline{u_\parallel}) \approx \overline{S(P,T,\chi_\alpha,u_\parallel)}, \tag{5}$$

where the overbar denotes the time-averaging operation.

Furthermore, the LIF model used herein has not been formally validated, makes Gaussian assumptions on the shapes of the laser spectral and absorption profiles (i.e., *triple-Gaussian assumption*[20]), and neglects the attenuation of the laser light intensity caused by absorption of NO. Under some circumstances, the absorption effect can be partially corrected by the image post-processing, as noted during the PLIF image postprocessing discussion. However, for the current experiments, any off-image absorption due to the laser light passing through the optically inaccessible, NO-filled, test cabin can not be corrected and is difficult to quantify. Furthermore, for those images where absorption could not be effectively corrected in post-processing (e.g., Fig. 19) because various rates of absorption are observed in the image, an approach motivated by the Beer-Lambert law[48,49] was used to model the absorption effect. This absorption model was not applied directly to the computed LIF signal, but rather used as an image processing filter that attenuated the normalized gray scale intensity (i.e., black-to-white is zero-to-one) of the resulting CFI images. As such, each pixel in the CFI image was scaled by the intensity attenuation parameter, D, which is the ratio of "transmitted" to "incoming" LIF image intensity:

$$D = \frac{I_t}{I_i} = C_1 Exp(-\tau) \tag{6}$$

where I_i, I_t, and τ are the incident and transmitted image intensity, and the optical depth, respectively. The optical depth is further defined as:

$$\tau = C_2 \int_0^l I(z) dz \tag{7}$$

where the integral is evaluated over the optical path. The above equations contain two constants, C_1 and C_2, which can be adjusted to tune the level of absorption in CFIs to that visually observed in the experiment. In the current work, the constants C_1 and C_2 are set to one, and varied between 1 to 3, respectively. The latter adjustments are needed because the current CFD assumes that an infinitely wide array of injectors is a good numerical representation of the finite-width injector array. Given this assumption, even a more complex and quantitative absorption model, if applied here to obtain the CFI, would still require some tuning to account for absorption in the optically inaccessible cabin portion of the flowfield.

RESULTS AND DISCUSSION

Figure 22 shows the schlieren images obtained experimentally and from the CFD. The experimental data were obtained for the strut injector at high total enthalpy conditions under unfueled, and fueled conditions with an ER of 0.5, 1.0, and 1.5. The goal of the schlieren imaging was to provide preliminary visualization and determine the sensitivity of the technique to various fueling levels. Clear differences can be observed in Fig. 22, between unfueled and fueled experiments. However, obvious discernible differences cannot be observed among the grossly different fueling levels, thus rendering these visualizations of limited use. This is likely due to the fairly long line-of-sight for the current experiments and the fact that multiple injectors are used, thereby adding an ensemble averaging element to the line-of-sight integration. Nevertheless, the schlieren technique provides valuable preliminary visualization of the flow features and the target operating conditions via measurements of the observed shock wave angles. The synthetic schlieren image obtained from the CFD data for ER of 1.0 is shown in Fig. 22(e). This image is qualitatively very similar to those obtained experimentally for all the fueled cases. Contour plot of the vertical density gradient on a single streamwise plane through the strut injector centerline is also shown to highlight the impact and the importance of the line-of-sight averaging on the synthetic schlieren visualizations.

Figures 23–28 show comparisons between the time-averaged PLIF images and the corresponding computationally derived PLIF (termed CFI) obtained for different fuel injectors and using different sets of LIF transition lines. Figure 23 shows the time-averaged streamwise images obtained along the centerline of the strut injector block and cutting through the middle injector. The injector body is partially visible in the top-left section of the images with the dark regions representing fuel plumes emanating from the four injector body fuel ports. The laser sheet travels from bottom to top of the image. As expected, both the experiment and the CFI are sensitive to not only the NO concentration (recall that there is no NO in the fuel simulant stream) but also to temperature and pressure. Both images are obtained by probing and modeling the LIF from the $^{\mathrm{S}}\mathrm{R}_{21}(9.5) + \mathrm{Q}_1(20.5) +^{\mathrm{Q}} \mathrm{P}_{21}(20.5) + \mathrm{R}_2(18.5)$ transition lines. The qualitative comparison appears reasonable with many of the flow features visible in both the PLIF images and the CFI. No absorption modeling is applied to the CFI here because little is observed in the post-processed PLIF. The CFI generally appear to have greater contrast as compared to the PLIF. One reason for this may be that steady RAS assumes that all fluctuations are turbulent in nature and lacks the “smoothing” effects associated with time-averaging of intrinsically unsteady large or discreet flow features. This effect is, in general, most pronounced for the discrete flow features like shocks. The darker image regions that are the fuel plumes also appear to persist farther downstream in the CFI than PLIF image. This would seem to indicate a greater degree of mixing in the experiments than in the CFD. However, this slight discrepancy could be the result of modeling errors in the CFI, and the flow condition differences between the experiment and the CFD since the latter was obtained pretest. Furthermore, it should also be noted that no attempts have been made to calibrate the turbulence model parameters used in the CFD, most notably the turbulence Schmidt number, to improve the visual predictions of the mixing flowfield.

Figure 24 shows several time-averaged cross-stream PLIF images (left-most column), CFI (two middle columns), and the mass fraction of air (right-most column) obtained for the strut injector. The image planes are located at 0.5, 1.0, 2.0, 4.0, and 6.0 inches downstream from the injector face, respectively. The laser sheet travels from left-to-right in these images. It should also be noted that the PLIF images have been cropped here to focus on the injector flowfield and match the visual extent of the CFI. The PLIF and the

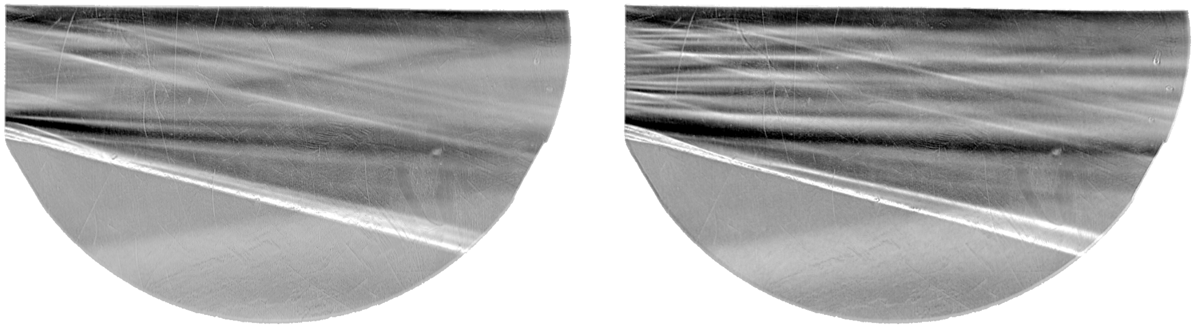

(a) Unfueled

(b) ER=0.5

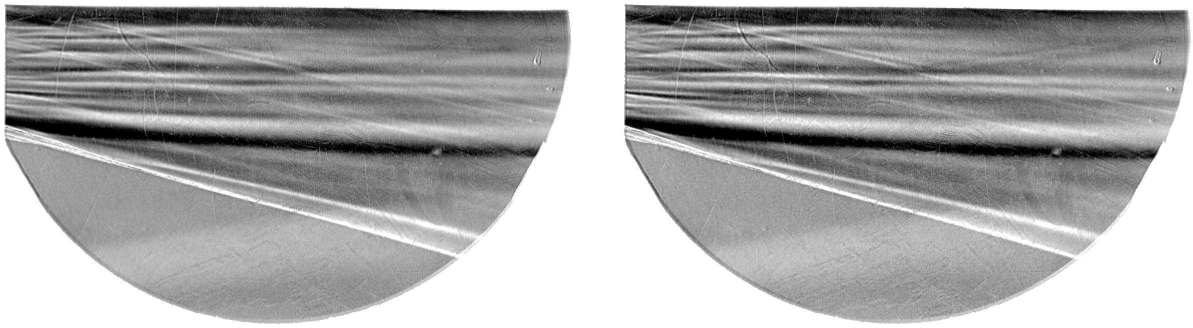

(c) ER=1

(d) ER=1.5

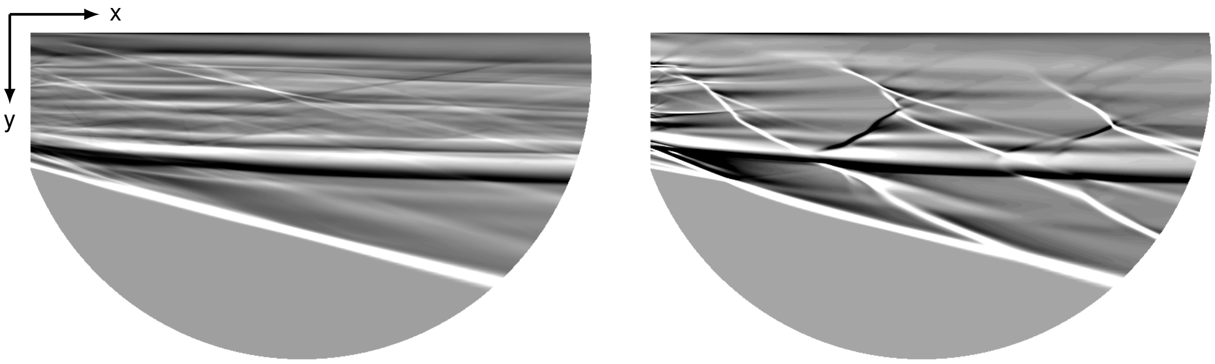

(e) ER=1.0; Synthetic schlieren (i.e., line-of-sight average of the vertical density gradient obtained from the CFD simulation).

(f) ER=1.0; Contours of the vertical density gradients on a single streamwise plane through the center of the strut injector obtained from the CFD.

Figure 22. Time-averaged experimental schlieren images for the strut injector obtained at various equivalence ratios (a-d), and the synthetic schlieren image (e) and contours of the vertical density gradient on a single streamwise plane (f) obtained from the CFD simulation.

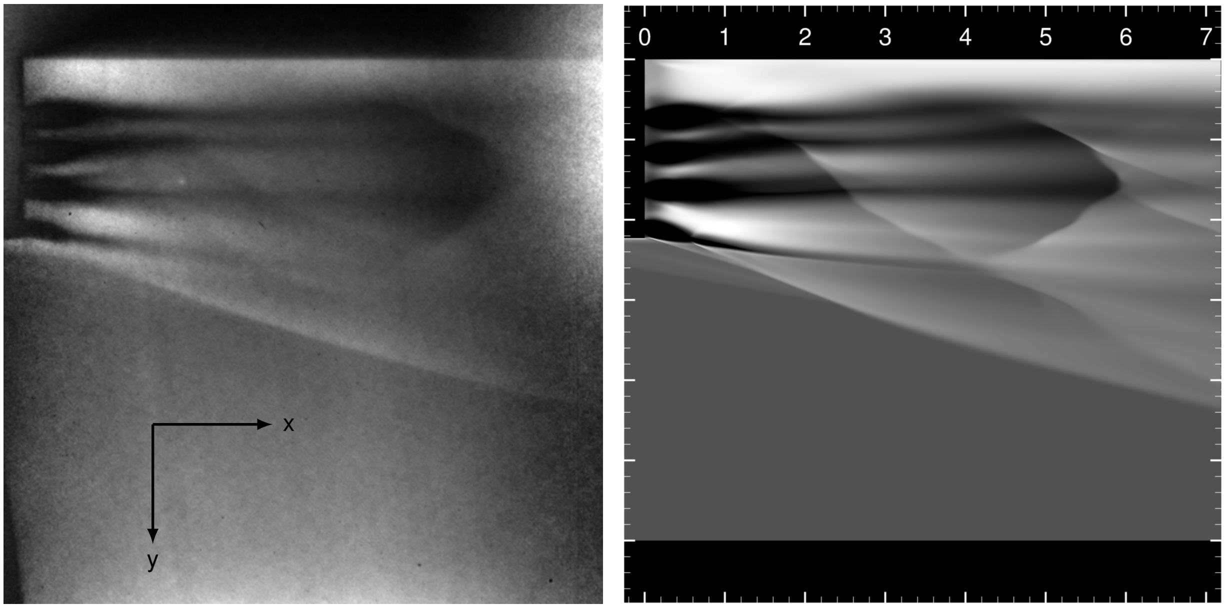

Figure 23. Time-averaged streamwise PLIF image (left) through the center of the strut injector and the corresponding CFI (right). The dimensions are in inches.

CFI are obtained using the mass-fraction-sensitive, $^{\mathrm{O}}\mathrm{P}_{12}(6.5) +^{\mathrm{O}} \mathrm{P}_{12}(14.5)$, transition lines. The left and right central columns of the CFI show images with the laser tuned to the 14.5 and 6.5 lines, respectively. The intent of the diagnostic approach was to tune the laser to the 6.5 line to improve the correlation of the LIF with the mass fraction of helium (shown on the right-most column). However, because these lines are positioned within one FWHM of the laser linewidth from one another, and have grossly different rotational quantum numbers and absorption characteristics, tuning of the laser to a specific line may have proved challenging during the experiments. Since there is no (or little) Doppler-shift effect present in the PLIF images, it can be safely assumed that the laser is indeed well-tuned to one of these lines, and so it is possible that the laser was actually tuned to the 14.5 line in the experiments. The CFI for this latter line produces a much closer visual match to the PLIF and a reasonable overall qualitative agreement. It should be noted that it is also possible that the CFI modeling at the lower values of the rotational quantum numbers introduces significant errors into the CFI. Both hypotheses are equally likely because the PLIF models have not been formerly validated. In addition, some of the differences between the PLIF and CFI could also be the result of slight differences in the facility air Mach number and the ratio of specific heats between the experiment and the CFD (recall that CFD was performed pretest). Some “edge” effects are also visible in PLIF images at the farthest downstream location. These manifest themselves through the distortions to the shock patterns near the left and right edges of the images. These edge effects are absent from the CFI, which utilizes RAS data with symmetry boundary conditions that effectively simulate an infinite row of injectors.

Several shockwave patterns, visible in the gaps between the injectors at the 0.5 and 1.0 inch locations in Fig. 24, appear distinctly different between the PLIF and CFI images. This difference is attributed to the underprediction in the size of the shock-induced flow separation on the strut injector body side in the CFD simulations. Figure 25(a) shows the strut injector body with the isosurface of the streamwise velocity of 800 m/s, and the spanwise and cross-stream planes with contours of synthetic shadowgraph obtained from the CFD. The contours of the shadowgraph on the spanwise plane reveal that the oblique shock wave from the adjacent injector leading edge impacts the strut injector side and induces flow separation, which is visible as a small, diagonally-running, “hill” in the streamwise velocity isocontour in Fig. 25(a). This flow separation leads to a double shock reflection, which manifests itself as “double line” on both the

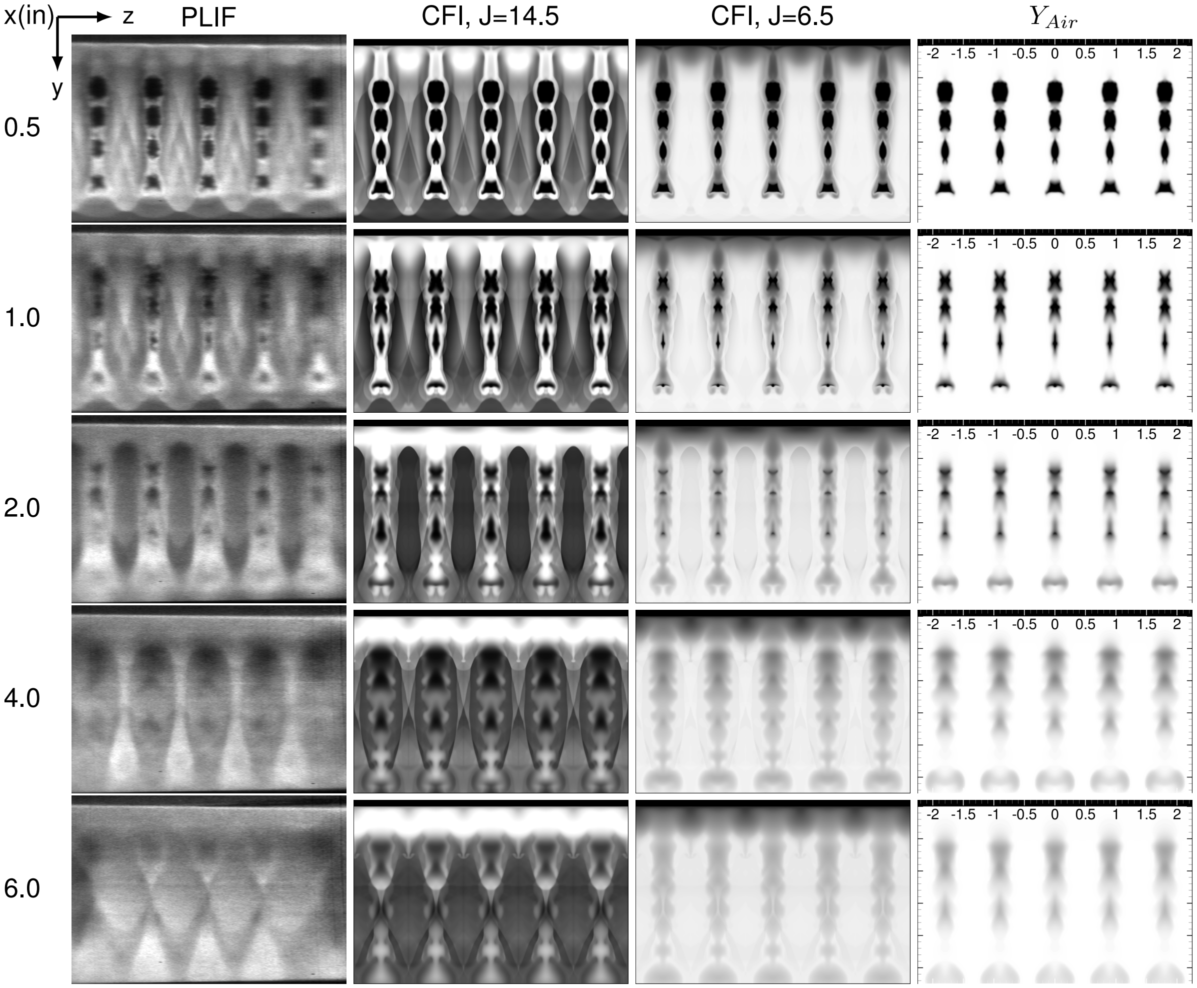

Figure 24. Time-averaged cross-stream PLIF images (left-most column) for the strut injector, the corresponding CFI (two middle columns), and mass fraction of air (right-most column) at 0.5, 1.0, 2.0, 4.0, and 6.0 inches (top-to-bottom) downstream from the injector face. The two middle CFI are obtained using the mass-fraction-sensitive LIF transition lines, with the left set of images corresponding to LIF where some laser detuning was allowed. The dimensions are in inches.

spanwise and cross-stream shadowgraphs. Figures 25(b,c,d) show the cross-stream PLIF and CFI images at 0.5 inches downstream of the injector trailing edge. It should be noted that the PLIF and CFI images have been rotated such that their y-axes are pointing up for visual consistency with the orientation of the CFD. In the PLIF image, shown in Fig. 25(b), these double lines are circled, and are spaced farther apart than the same double lines outlined in the CFI, shown in Fig. 25(c). The larger spacing in the PLIF image, indicates that the flow separation “hill” is larger in the experiments. This is not necessarily surprising given that it is likely that the boundary layer flow over the upstream portions of the strut injector body is laminar or transitional, and only becomes fully turbulent downstream of the shock impingement location, whereas this flow is modeled as fully turbulent, and therefore, more resilient to flow separation, in the current CFD. The CFI obtained from a fully laminar CFD simulation is shown in Fig. 25(d). It is clear that the double shock reflections match those found in the PLIF images, supporting above assertion, however, without the turbulence model to augment the fuel-air mixing, the fully laminar CFD simulations are expected to significantly underpredicted the mixing efficiency.

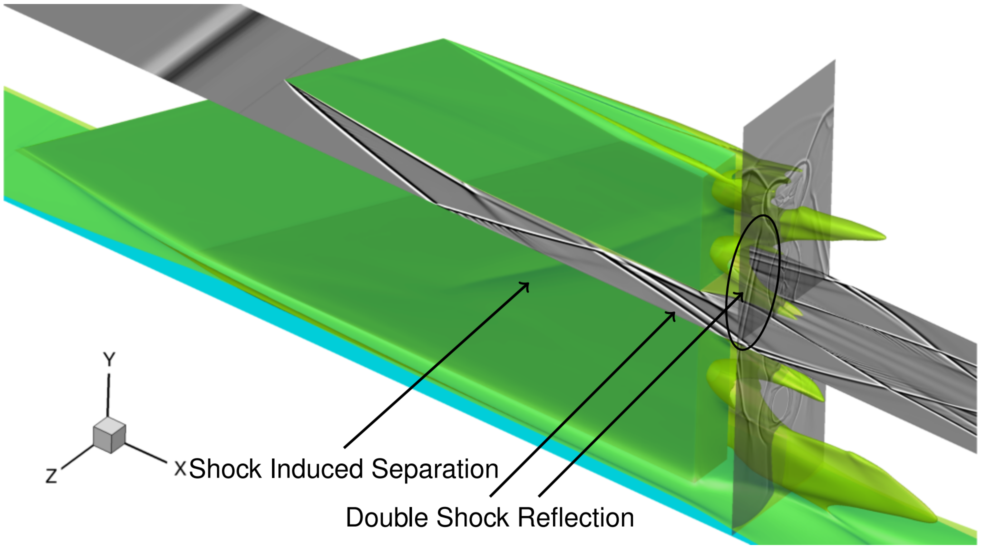

(a) Isocontour of the streamwise velocity of 800 m/s, and contours of the synthetic shadowgraph on the spanwise (y=1.18 in.) and cross-stream (x=0.5 in.) planes obtained from the CFD solutions for the strut injector.

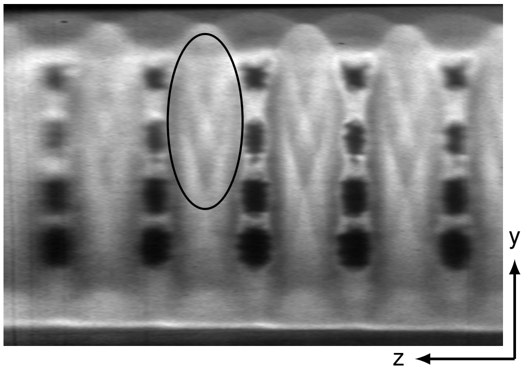

(b) PLIF at x=0.5 in. obtained using mass-fraction-sensitive LIF transition lines.

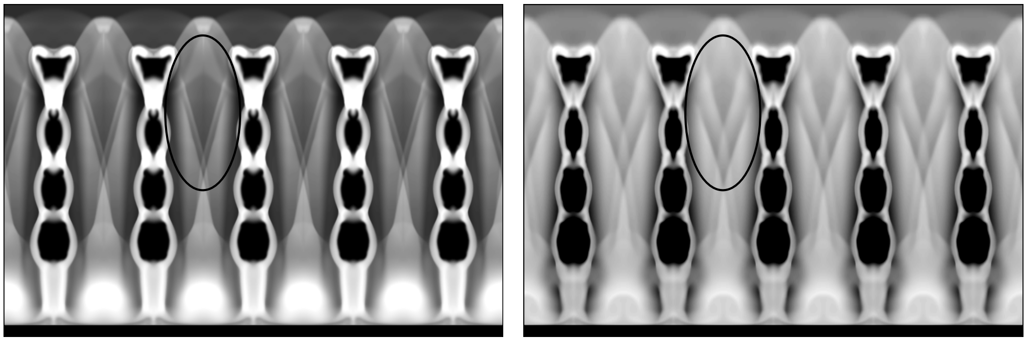

(c) CFI for J=14.5 at x=0.5 in.

(d) CFI of (c) obtained from a laminar CFD simulation

Figure 25. Isocontour of the streamwise velocity, and contours of the synthetic shadowgraph on the spanwise and cross-stream planes obtained from the CFD solutions for the strut injector (a), and the cross-stream PLIF (b) and CFI images (c,d) with the double shock reflection circled.

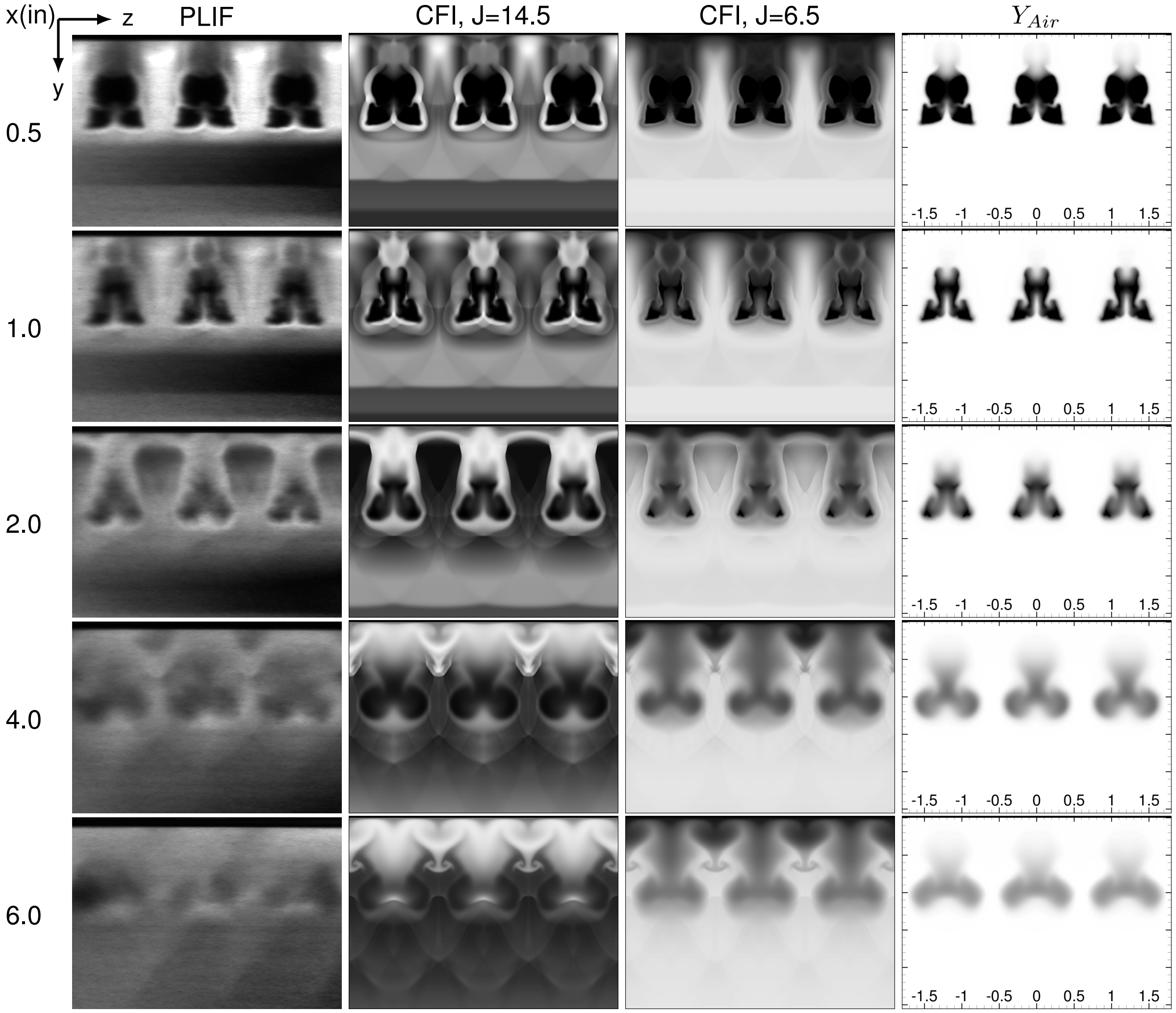

Figure 26. Time-averaged cross-stream PLIF images (left-most column) for the ramp injector, the corresponding CFI (two middle columns), and mass fraction of air (right-most column) at 0.5, 1.0, 2.0, 4.0, and 6.0 inches (top-to-bottom) downstream from the injector face. The two middle CFI are obtained using the mass-fraction-sensitive LIF transition lines, with the left set of images corresponding to LIF where some laser detuning was allowed. The dimensions are in inches.

Figure 26 shows several time-averaged cross-stream PLIF images (left-most column), CFI (two middle columns), and the mass fraction of air (right-most column) obtained for the ramp injector. The downstream locations are the same as those shown for the strut injector in Fig 24. The PLIF and the CFI are also obtained using the mass-fraction-sensitive transition lines, and the left and right of the two central columns of the CFI show the effect of tuning the laser to either the 14.5 or 6.5 line, respectively. Similar to above, the CFI of the LIF signal corresponding to the 6.5 line exhibits significantly less sensitivity to pressure and temperature, and makes the LIF signal compare well visually with the mass fraction of air shown in the right-most column. However, once again, it is the CFI corresponding to the 14.5 line that produces a closer visual match to the PLIF images. The qualitative agreement between the PLIF and latter CFI is similar to that observed for the strut injector. However, notable in the PLIF images is the absorption of signal in the shock layer just below the ramp injector bodies. This absorption is a result of rapid depletion of the light energy due to the increase in both temperature and pressure inside the shock layer. The absorption observed in this shock layer was not completely corrected by the PLIF image postprocessing because the

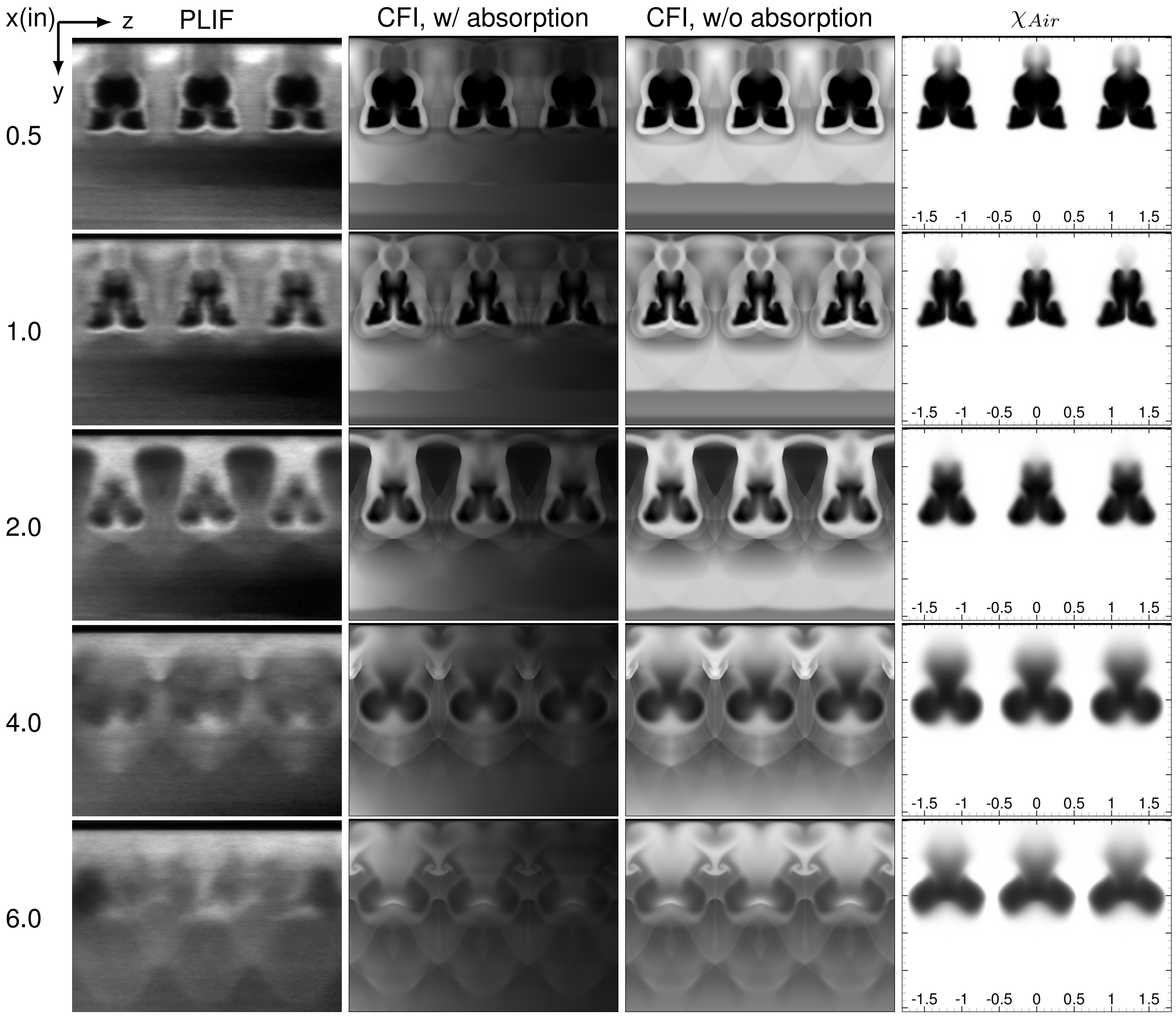

Figure 27. Time-averaged cross-stream PLIF images (left-most column) for the ramp injector, the corresponding CFI (two middle columns), and mole fraction of air (right-most column) at 0.5, 1.0, 2.0, 4.0, and 6.0 inches (top-to-bottom) downstream from the injector face. The two middle CFI are obtained using the mole-fraction-sensitive LIF transition lines, with the left set of images corresponding to LIF where Beer-Lambert absorption model was applied to the CFI on the right. The dimensions are in inches.

absorption rate is greater than that outside of the shock layer for which the image postprocessing was tuned. Although the absorption effect is unmodeled in the CFI, it can be approximated using the Beer-Lambert law, as shown next.

Figure 27 also shows several time-averaged cross-stream PLIF images (left-most column), CFI (two middle columns), and the mole fraction of air (right-most column) obtained for the ramp injector. The downstream locations are the same as before. However, the PLIF and the CFI are obtained using the mole-fraction-sensitive transition lines: ${}^{\mathrm{R}}\mathrm{Q}_{21}(12.5) + \mathrm{R}_1(12.5)$. These “double lines” are easier to tune to, and are not sensitive to small laser detuning because they are much closer to each other in the spectral space (about $0.04\,\mathrm{cm}^{-1}$) and have the same rotational quantum number. The left of the two central columns of the CFI includes a simple absorption model as described in the fluorescence modeling section above. This model does qualitatively reproduce the left-to-right laser light absorption pattern. However, although the level of attenuation is proportional to signal strength, the entire CFI is clearly darker left-to-right, whereas the PLIF images seem only to exhibit absorption in the shock layer below the ramp injector body. This is somewhat expected because the absorption in the PLIF images has been partially corrected by the image postprocessing approach. Furthermore, the left-to-right absorption pattern in the CFI is also similar to the absorption patterns observed in the raw PLIF images (e.g., Fig. 16). The CFI without the absorption model is also shown in the right of the two central columns. Because the fuel simulant (helium) molecular weight is lower than that for air, the mole fraction of helium in the air mixture persists at high values downstream as compared to the mass fraction. This can be directly noted in the contours of the mole fraction of air, where the dark regions representing helium persist further downstream. Although the mole-fraction-sensitive lines also exhibit significant pressure and temperature sensitivity, it is still observed that the fuel plume shape and size are well correlated with the mole fraction of air. The qualitative agreement between the PLIF and CFI is similar to that observed above.

Figure 28 shows several time-averaged cross-stream PLIF images (left-most column), CFI (two middle columns), and the mole fraction of air (right-most column) obtained for the flushwall injector. The image planes are located at -1.0, -0.62, -0.12, 0.38, 1.38, 2.38, 3.38, and 4.38 inches (top-to-bottom) from the trailing edge of the rectangular injector port, respectively. Because the injector is 1.113 inches long, all the negative values represent planes that cross the injector opening. Due to the spatial constraints of the experimental article, only a single flushwall injector could be installed and imaged. However, as before, the CFD and the corresponding CFI effectively simulate an infinite row of injectors. Nevertheless, a direct comparison can still be made between PLIF and CFI as long as the compressible features (i.e., shocks and expansions) of neighboring injectors do not strongly interact. This is the case for all but the two most downstream image planes. Furthermore, the flushwall injector in the CFD is shifted about 1.49 inches downstream with respect to its experimental location. This shift is also a result of spatial restrictions on the experimental article that were unforeseen during the pretest CFD campaign. The only consequence of this shift, however, is that the bow shock emanating from the leading edge of the flat plate appears closer to the plate (top edge of each image) in the PLIF images than the CFI. The boundary layer thickness does not significantly change over that shift distance, therefore, it is not expected to significantly impact the results either. The PLIF and the CFI are obtained using the mole-fraction-sensitive transition lines. As above, a simple absorption model is used for the images in the left of the two central columns. This model does reproduce the characteristics absorption “shadows” visible to the right of the growing shock layer in the PLIF images. The CFI without this absorption model are shown on the right of the two central image columns. The qualitative agreement between the PLIF and CFI is similar to that observed above. However, one notable difference is the attenuation (darkening) of the CFI signal as the flow approaches the wall in the boundary layer. This attenuation is missing in all of the PLIF images. The cause of this effect is the difference in the flat plate surface temperature between the experiment and the CFD. In the experiments, the temperature measured with the surface thermocouples reaches about 340 K, whereas in the pretest CFD the plate surface was modeled using an adiabatic wall assumption resulting in the surface temperatures of about 900 K. Because the fluorescence signal is inversely proportional to the temperature, while Boltzmann fraction increases with the temperature for low temperatures then decreases, there exists a temperature for which the signal peaks, then decays as the temperature continues to increase (see appendix). For the mole fraction lines, the CFI equation reveals that the temperature for which the signal peaks is about 300 K, which is consistent with PLIF images of the boundary layer.

For the flushwall injector, the entrainment of air into the core of the fuel plume appears greater in the CFI than PLIF as evidenced by the larger extent of the signal inside the fuel plume. It also appears that the shock interactions with the neighboring injectors cause the fuel plume to “squeeze” and stretch downward, thereby increasing the fuel penetration slightly.

Figure 29 shows comparisons between the CFI and the reconstructed streamwise PLIF images. The reconstruction procedure uses cross-stream PLIF data previously shown in Fig. 24. All of the image postprocessing steps previously discussed, except the time-averaging, have been applied to individual PLIF images prior to performing the reconstruction procedure. The streamwise PLIF planes were constructed through the centers of the three center-most strut injectors, and the two midplanes between the center and

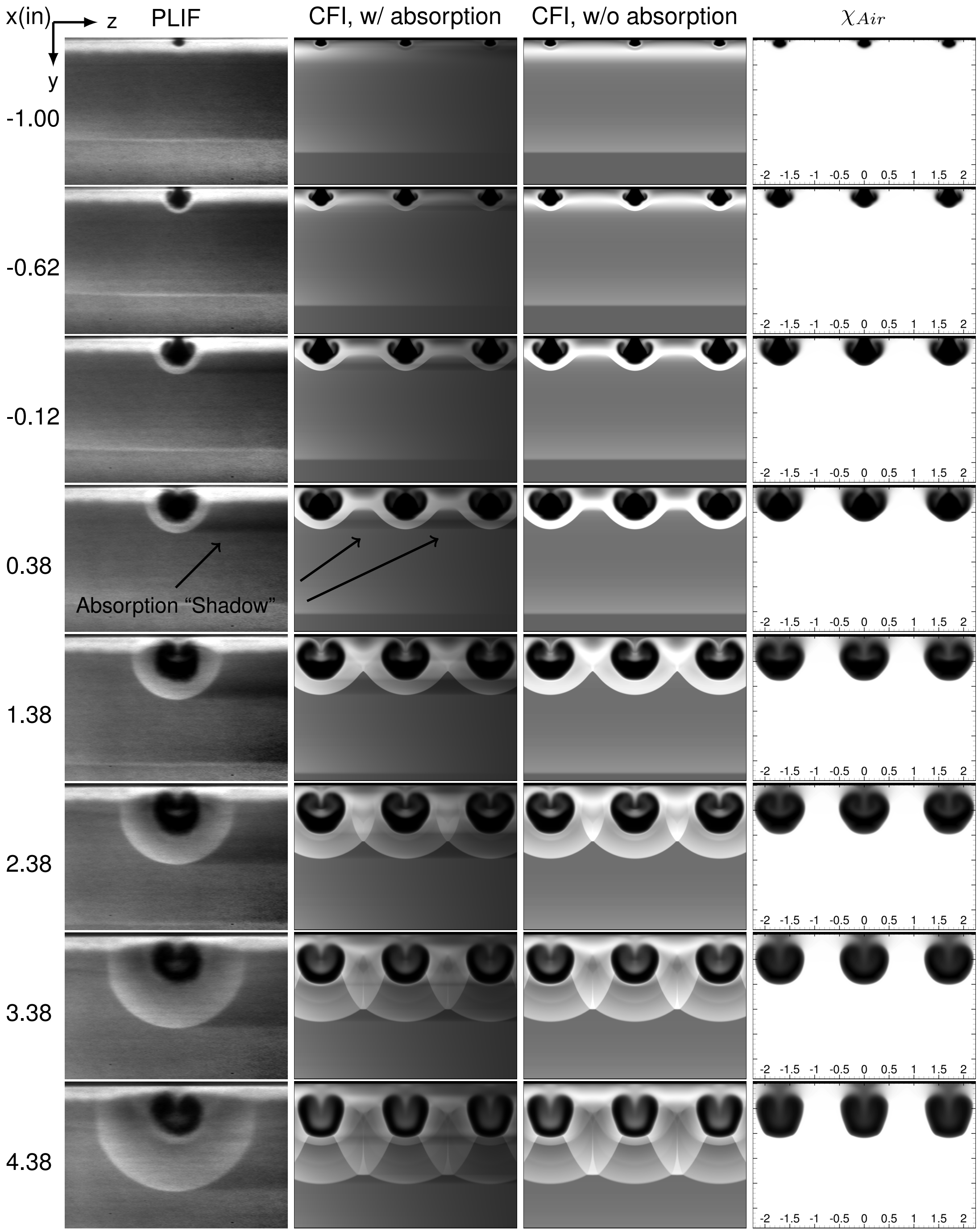

Figure 28. Time-averaged cross-stream PLIF images (left-most column) for the flushwall injector, the corresponding CFI (two middle columns), and mole fraction of air (right-most column) at -1.0, -0.62, -0.12, 0.38, 1.38, 2.38, 3.38, and 4.38 inches (top-to-bottom) from the injector trailing edge. The two middle CFI are obtained using the mole-fraction-sensitive LIF transition lines, with the left set of images corresponding to LIF where Beer-Lambert absorption model was applied to the CFI on the right. The experimental PLIF images contain only one injector whereas the CFD modeled a row of injectors. The dimensions are in inches.

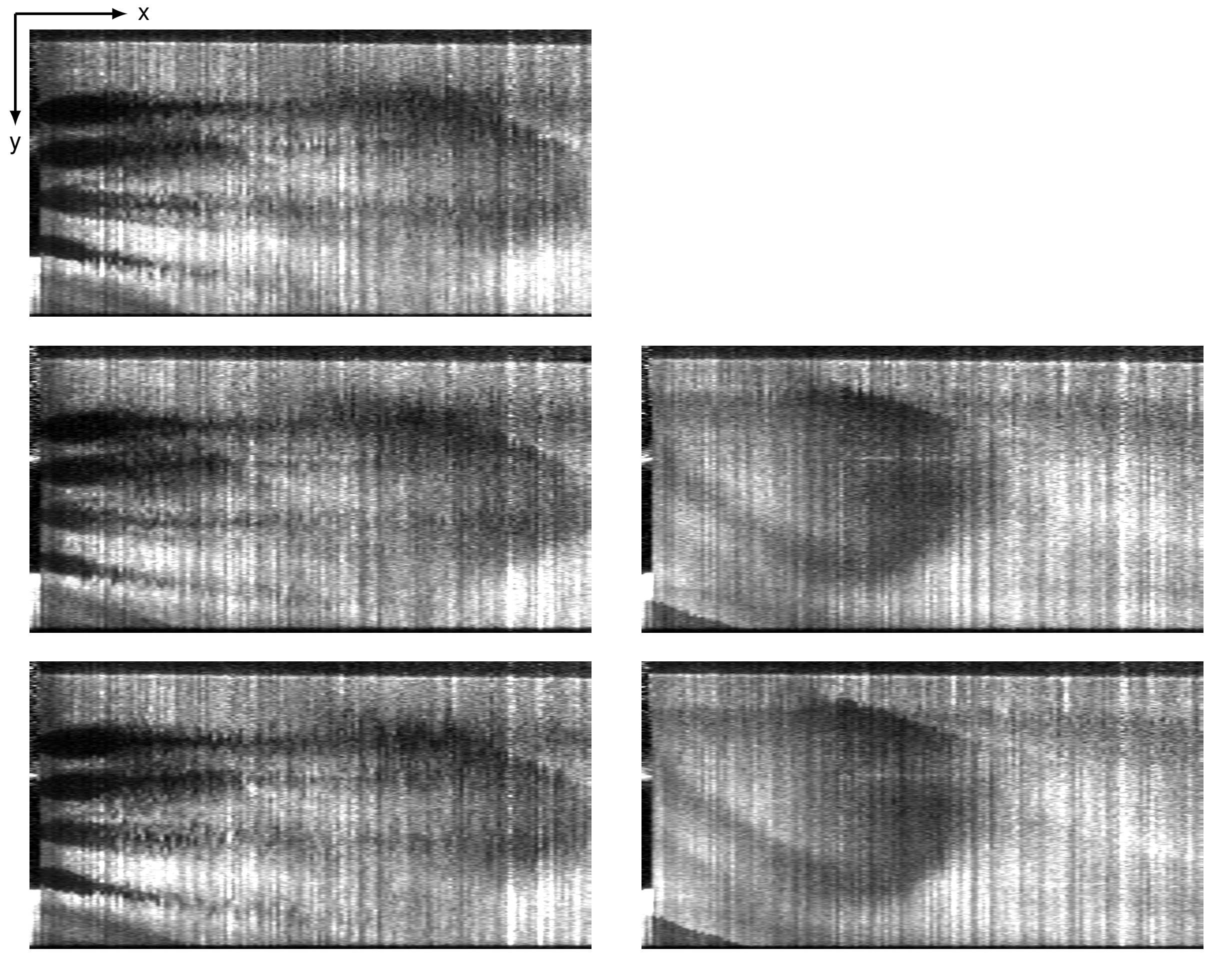

(a) Reconstructed streamwise PLIF images through the centers of the three center-most strut injectors.

(b) Reconstructed streamwise PLIF images through the mid-plane between the center and two adjacent strut injectors.

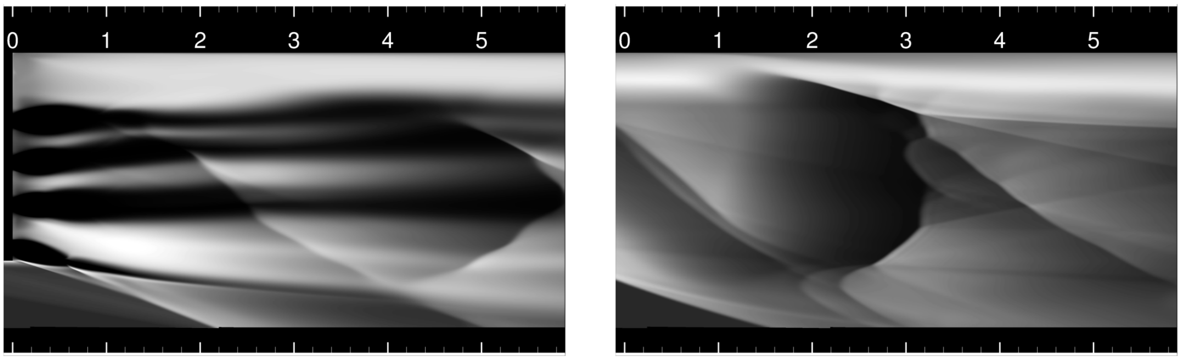

(c) Streamwise CFI images through the center of the strut injector.

(d) Streamwise CFI images through the midplane between the adjacent strut injectors.

Figure 29. Reconstructed streamwise PLIF images obtained through the centers of the three center-most strut injectors (a), and the midplanes between the center and two adjacent strut injectors (b), and their corresponding CFI (c), (d). The reconstruction is based on instantaneous PLIF images obtained using the fastest laser sheet translation rate of 0.4 inches per second. All images are obtained using the mass-fraction sensitive LIF transition lines.

two adjacent strut injectors. Whereas Fig. 24 shows the time-averaged PLIF, the current reconstruction is based on the instantaneous PLIF images obtained using the laser sheet translation rate of 0.4 inches per second. With this translation rate, each reconstructed pixel is scaled and interpolated in the streamwise dimension by a factor of about 5.8 to recover the proper physical dimension and aspect ratio of the reconstructed image. Qualitatively, the reconstructed PLIF and the CFI reproduce similar flow features as those previously observed. However, the fidelity of the reconstructed PLIF images is visibly lower than that of the time-averaged PLIF images. Specifically, shot-to-shot intensity variations in the instantaneous source PLIF data are clearly visible via the changing brightness of the vertical lines. The observed level of shot-to-shot intensity variation still remains, even after applying the postprocessing normalization discussed earlier (see Fig. 17). Also notable are some of the fluctuating turbulent features that manifest themselves as random patches in the streamwise and cross-stream directions (see Fig. 29(a)). These patches can be observed near the helium-air mixing interfaces (i.e., edges of the black regions) and near the edge of the boundary layer. Although these features are real representations of the underlying turbulence as captured by PLIF, because the source cross-stream PLIF data are temporally uncorrelated, these features effectively appear random, and for the current case, are enlarged by the postprocessing in the streamwise direction. Nevertheless, these randomized flow features do provide some additional, qualitative visualizations about the extent of the turbulence fluctuations near the mixing interfaces between helium and air and at the edge of the boundary layer.

Figure 30 shows comparisons between the reconstructed PLIF and the corresponding CFI, using the same source data as in Fig. 29 but reconstructing the spanwise (i.e., xz-planes) instead of streamwise (i.e., xy-planes) planes. The three spanwise planes were obtained through the centers of the three parallel fuel ports of the strut injector. Qualitatively, the reconstructed PLIF and the CFI produce similar flow features.

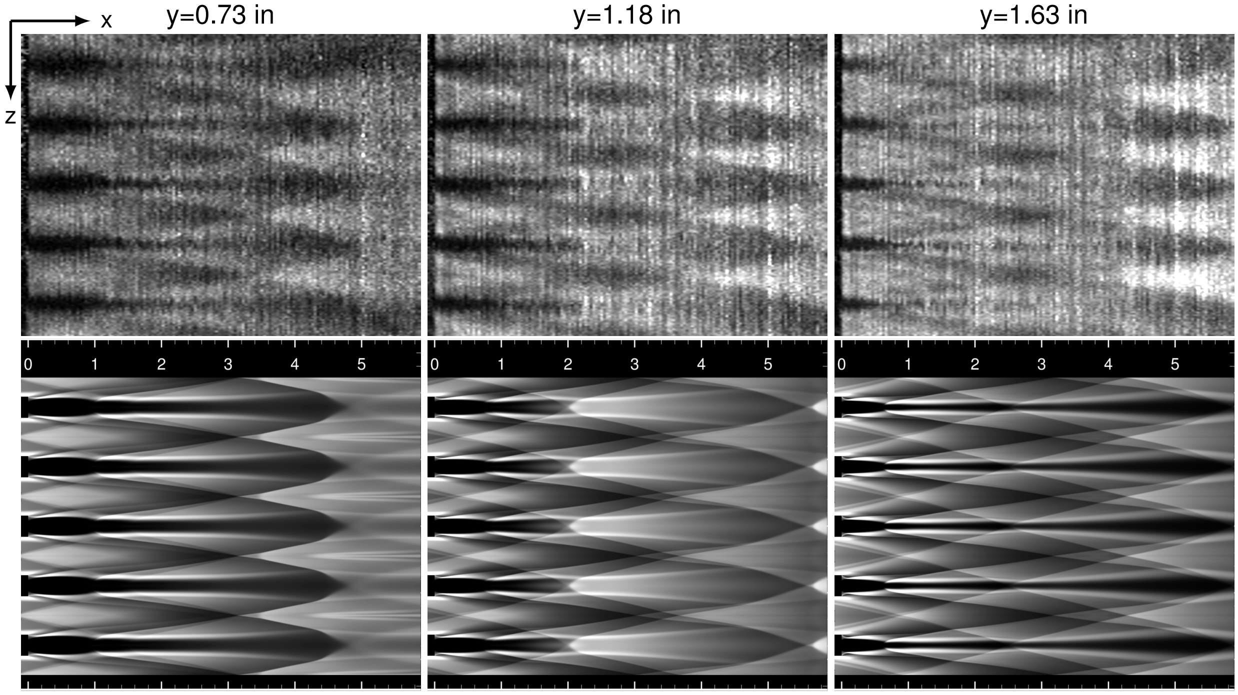

Figure 30. Reconstructed spanwise PLIF images obtained through the centers of the three parallel fuel ports of the strut injector (top row), and the corresponding CFI (bottom row). From left-to-right, each plane corresponds to the fuel port that is the closest and farthest away from the flat plate, respectively. The reconstruction is based on instantaneous PLIF images obtained using the fastest laser sheet translation rate of 0.4 inches per second. All images are obtained using the mass-fraction sensitive LIF transition lines.

More specifically, the position and the extent of the fuel streaks, and the shock "triangle" flow features are captured by the CFI. However, all of the caveats discussed above apply.

Figure 31 shows comparisons between the CFI and the reconstructed PLIF images for the flushwall injector for two different values of the laser sheet translation rate of about 0.13 and 0.07 inches per second. The current reconstruction procedure uses cross-stream PLIF data obtained using mole-fraction sensitive LIF transition lines, and collected at lower laser sheet translation rates for the purpose of obtaining improved resolution in the 3D reconstruction. However, because the total experimental run time could not be easily increased during the slower translation experiment, the laser sheet reached only about half the downstream distances as compared to the faster translation experiment. Given the two translation rates, each reconstructed pixel is scaled and interpolated in the streamwise dimension by a factor of about 1.95 and 0.97, for the faster and slower rate, respectively, to recover the proper physical dimension and the aspect ratio of the reconstructed image. For the slower translation experiment, the scale factor is slightly less than one indicating that the image resolution in both cross-stream and the reconstructed streamwise directions are nearly the same. The streamwise plane, shown on the left column of Fig. 31, was obtained through

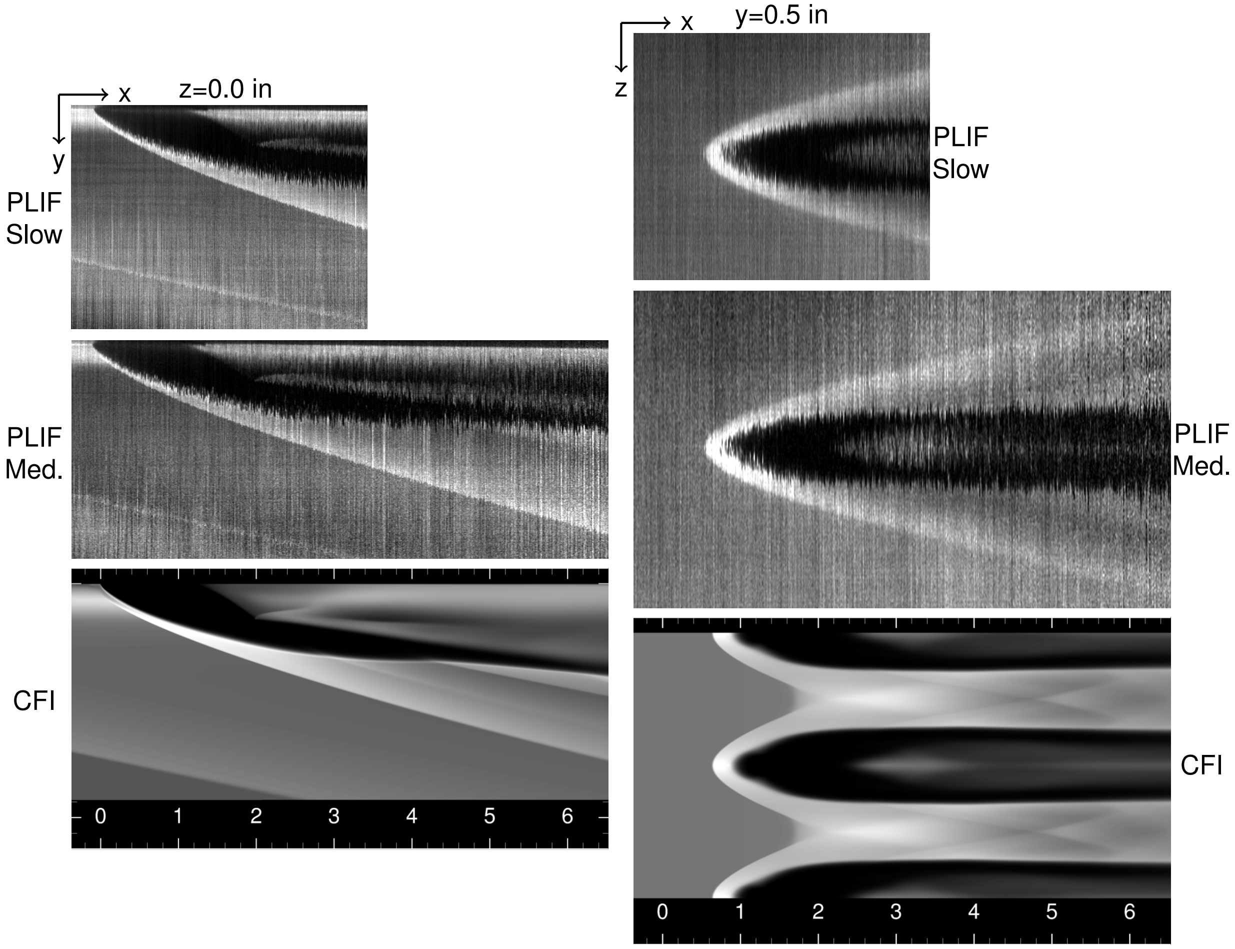

Figure 31. Reconstructed streamwise PLIF images obtained through the center of the flushwall injector (left), and the spanwise plane located 0.5 inches from the flat plate (right), and the corresponding CFI (bottom). The reconstruction is based on instantaneous PLIF images obtained using the slowest (top) and medium (middle) laser sheet translation rate of 0.0668 and 0.1336 inches per second, respectively. All images are obtained using the mole-fraction sensitive LIF transition lines.

the center of the flushwall injector, whereas the spanwise plane, shown on the right, was obtained at a distance of 0.5 inches from the flat plate. For both the slow and fast translation runs, the fidelity of the reconstructed images is improved as compared to that observed for the strut injector in Figs. 29 and 30. Both the general shockwave and flow features are also comparable between PLIF images and the CFI. The turbulent flow features, randomized by the reconstruction procedure as discussed previously, are also much more clearly noted. It is interesting to further note that the shock features also exhibit these randomized features but at a much lower amplitude, indicating that shocks are relatively steady as compared to the fuel-air mixing interfaces. Not surprisingly, these results suggest that the slower translation rate is preferred if 3D reconstruction is to be considered, with the laser sheet translation rate adjusted so as not to exceed a scaling factor of about 2. Furthermore, scaling factors of much less than one would require much longer experimental run times, however, these low scaling factors do offer a potential for effectively obtaining a time-averaged equivalent for a 3D reconstructed image. That is, for small scaling factors, multiple source lines would be combined through the scaling and interpolation process into a single “average” line. For example, if the laser sheet translation rate for the current experiment was set to 0.002 inches per second, then the scaling factor needed for image reconstruction would be about 0.03, which would effectively cause “compressing” instead of stretching of about 30 source lines into a single one during the reconstruction process, thereby producing an equivalent time-averaging effect. However, to examine a distance of 6 inches downstream of an injector would require an experimental run time of about 50 minutes, and would produce about 30000 cross-stream PLIF images.

SUMMARY AND CONCLUSIONS

The current work compares the experimentally-obtained and CFD-computed NO PLIF images of the mixing flowfields for three high-speed fuel injectors, with helium used as an inert substitute for hydrogen fuel. The three injectors include a strut, a ramp, and a high aspect ratio rectangular flushwall injector. These devices accomplish the task of distributing and mixing fuel into the supersonic crossflow, albeit via different strategies. Both schlieren and PLIF techniques are applied to obtain mixing flowfield flow visualizations. The schlieren technique produced no discernible differences among the grossly different fueling levels, thus rendering these visualizations of limited use. The experimental PLIF is obtained by using a UV laser sheet to interrogate a plane of the flow by exciting fluorescence from the NO molecules that are present in the Arc-Heated Scramjet Test Facility at NASA Langley. Because the NO is present in the facility air, the absence of signal is an indication of pure fuel. Three different sets of fluorescence transition lines are used in the current work. Each set of lines exhibits different sensitivity to pressure, temperature, and mixture composition, and has different absorption characteristics. Two of the transition lines have been selected for their linear correlation with either mass fraction or mole fraction of helium. However, the mass-fraction sensitive LIF transition lines proved challenging to work with in practice because of the close spectral proximity of another line. The computed PLIF images are obtained by applying a weak excitation fluorescence model for NO to the results of the Reynolds-averaged simulations carried out using the VULCAN-CFD solver. This process is called computational flow imaging (CFI). This approach is required because the PLIF signal is a nonlinear function of not only NO concentration, but also pressure, temperature, and the flow velocity. Although this complexity makes it difficult to directly obtain more common aerothermodynamic properties, such as pressure, temperature, species concentration, and flow velocity, it does allow for additional, composite, flow features to be identified and compared with the CFD. However, such comparisons are only semiquantitative. The semiquantitative nature of the comparisons stems from the uncertainties in the instantaneous amount of background NO, the absorption modeling, the PLIF signal postprocessing, as well as uncertainties in the PLIF signal modeling itself. The instantaneous PLIF images are also time-averaged. The laser energy absorption in the CFI is qualitatively modeled using a simple image postprocessing filter motivated by the Beer-Lambert law, and applied to the time-averaged images. Three-dimensional image reconstruction, similar to that used in magnetic resonance imaging, is also used to obtained streamwise and spanwise planes from the cross-stream PLIF data. Reasonable agreement is observed between all of the experimental visualizations and the CFI, establishing an increased confidence in the postprocessing and modeling approaches, and the CFD simulations.

ACKNOWLEDGMENTS

The authors would like to thank Stephen B. Jones for his help and advice with setting up the schlieren system in the AHSTF. This work is supported by the Hypersonic Technology Project in the Advanced Air Vehicles Program of the NASA Aeronautics Research Mission Directorate (ARMD). Experimental support was provided by the Supersonic and Hypersonic Testing Branch at the NASA Langley Research Center. Computational resources are provided by the NASA Langley Research Center and the NASA Advanced Supercomputing (NAS) Division.

REFERENCES

[1] Peebles, C., ***Road to Mach 10: Lessons Learned From the X-43A Flight Research Program***, Library of Flight Series, AIAA, Washington, D.C. (2008).

[2] Hank, J. M., Murphy, J. S., and Mutzman, R. C., ***The X-51A Scramjet Engine Flight Demonstration Program***, in *15th AIAA International Space Planes and Hypersonic Systems and Technologies Conference*, AIAA, Dayton, OH (May 2008).

[3] Lee, J., Lin, K.-C., and Eklund, D., ***Challenges in Fuel Injection for High-Speed Propulsion Systems***, AIAA J., 53(6):1405–1423 (Jun. 2015).

[4] Cabell, K., Drozda, T. G., Axdahl, E. L., and Danehy, P. M., ***The Enhanced Injection and Mixing Project at NASA Langley***, in *JANNAF 46th CS / 34th APS / 34th EPSS / 28th PSHS Joint Subcommittee Meeting*, Albuquerque, NM (Dec. 2014).

[5] Baurle, R. A., Fuller, R. P., White, J. A., Chen, T. H., Gruber, M. R., and Nejad, A. S., ***An Investigation of Advanced Fuel Injection Schemes for Scramjet Combustion***, in *36th Aerospace Sciences Meeting and Exhibit*, Reno, NV (Jan. 1998).

[6] Ogawa, H., ***Physical Insight into Fuel-Air Mixing for Upstream-Fuel-Injected Scramjets via Multi-Objective Design Optimization***, J. Propul. Power., 31(6):1505–1523 (2015).

[7] Drozda, T. G., Drummond, J. P., and Baurle, R. A., ***CFD Analysis of Mixing Characteristics of Several Fuel Injectors at Hypervelocity Flow Conditions***, in *52nd AIAA/SAE/ASEE Joint Propulsion Conference*, AIAA 2016-4764, AIAA, Salt Lake City, UT (Jul. 2016).

[8] Cabell, K. F. and Rock, K. E., ***A Finite Rate Chemical Analysis of Nitric Oxide Flow Contamination Effects on Scramjet Performance***, Tech. Rep. TP-2003-212159, NASA (2003).

[9] Hartfield, R. J., Abbitt, J., , and McDaniel, J. C., ***Injectant Mole-Fraction Imaging in Compressible Mixing Flows Using Planar Laser-Induced Iodine Fluorescence***, Opt. Lett., 16(16):850–852 (1989).

[10] Clemens, N. T. and Mungal, M. G., ***Large-Scale Structure and Entrainment in the Supersonic Mixing Layer***, J. Fluid Mech., 284:171–216 (1995).

[11] Island, T. C., Urban, W. D., and Mungal, M. G., ***Quantitative Scalar Measurements in Compressible Mixing Layers***, in *34th AIAA Aerospace Sciences Meeting and Exhibit*, AIAA, AIAA, Reno, NV (Jan. 1996).

[12] Donohue, J. M. and McDaniel, J. C., ***Computer-Controlled Multiparameter Flowfield Measurements Using Planar Laser-Induced Iodine Fluorescence***, AIAA J., 34(8):1604–1611 (1996).

[13] Fox, J. S., Houwing, A. F. P., Danehy, P. M., Gaston, M. J., Mudford, N. R., and Gai, S. L., ***Mole-Fraction-Sensitive Imaging of Hypermixing Shear Layers***, J. Propul. Power., 17(2):284–292 (2001).

[14] Gaston, M. J., Houwing, A. F. P., Mudford, N. R., Danehy, P. M., and Fox, J. S., ***Fluorescence Imaging of Mixing Flowfields and Comparisons with Computational Fluid Dynamic Simulations***, Shock Waves, 12:99–110 (2002).

[15] Rossmann, T., Mungal, M. G., and Hanson, R. K., ***Nitric-Oxide Planar Laser-Induced Fluorescence Applied to Low-Pressure Hypersonic Flow Fields for the Imaging of Mixture Fraction***, Appl. Opt., 42(33):6682–6695 (Nov. 2003).

[16] Rossmann, T., Mungal, M. G., and Hanson, R. K., ***Mixing Efficiency Measurements Using a Modified Cold Chemistry Technique***, Exp. Fluids, 37(4):566–576 (Aug. 2004).

[17] Takahashi, H., Ikegami, S., Oso, H., Masuya, G., and Hirota, M., ***Quantitative Imaging of Injectant Mole Fraction and Density in a Supersonic Mixing***, AIAA J., 46(11):2935–2943 (2008).

[18] Kidd III, F. G., Narayanaswamy, V., Danehy, P. M., Inman, J. A., Bathel, B. F., Cabell, K. F., Hass, N. E., Capriotti, D. P., Drozda, T. G., and Johansen, C. T., ***Characterization of the NASA Langley Arc Heated Scramjet Test Facility Using NO PLIF***, in *30th AIAA Aerodynamic Measurement Technology and Ground Testing Conference*, Atlanta, GA (Jun. 2014).

[19] Havener, G., ***Computational Flow Imaging: Fundamentals and History***, in *18th AIAA Aerospace Ground Testing Conference*, AIAA-94-2615, AIAA, Colorado Springs, CO (Jun. 1994).

[20] Ivey, C. B., Danehy, P. M., Bathel, B. F., Dyakonov, A. A., Inman, J. A., and Jones, S. B., ***Comparison of PLIF and CFD Results for the Orion CEV RCS Jets***, in *49th AIAA Aerospace Sciences Meeting*, AIAA-2011-713, AIAA, Orlando, FL (Jan. 2011).

[21] VULCAN-CFD, ***http://vulcan-cfd.larc.nasa.gov/*** (Dec. 2017).

[22] Drozda, T. G., Axdahl, E. L., and Cabell, K. F., ***Pre-Test CFD for the Design and Execution of the Enhanced Injection and Mixing Project at NASA Langley Research Center***, in *JANNAF 46th CS / 34th APS / 34th EPSS / 28th PSHS Joint Subcommittee Meeting*, Albuquerque, NM (Dec. 2014).

[23] Drozda, T. G., Cabell, K. F., Passe, B. J., and Baurle, R. A., ***Computational and Experimental Characterization of the Mach 6 Facility Nozzle Flow for the Enhanced Injection and Mixing Project at NASA Langley Research Center***, in *55th AIAA Aerospace Sciences Meeting*, AIAA 2017-1537, AIAA, Grapevine, TX (Jan. 2017).

[24] Brown, G. L. and Roshko, A., ***On Density Effects and Large Structure in Turbulent Mixing Layers***, J. Fluid Mech., 64:775–816 (1974).

[25] Bogdanoff, D. W., ***Compressibility Effects in Turbulent Shear Layers***, AIAA J., 21(6):926–927 (1983).

[26] Papamoschou, D. and Roshko, A., ***The Compressible Turbulent Shear Layer: An Experimental Study***, J. Fluid Mech., 197:453–477 (1988).

[27] Gruber, M. R., Nejad, A. S., and Dutton, J. C., ***Circular and Elliptical Transverse Injection into a Supersonic Crossflow – The Role of Large-Scale Structures***, in *26th Fluid Dynamics Conference*, San Diego, CA (Jun. 1995).

[28] Schetz, J. A. and Billig, F. S., ***Penetration of Gaseous Jets Injected into a Supersonic Stream***, J. Spacecraft. Rockets., 3(11):1658–1665 (1966).

[29] Mao, M., Riggins, D. W., and McClinton, C. R., ***Numerical Simulation of Transverse Fuel Injection***, in *Computational Fluid Dynamics Symposium on Aeropropulsion*, NASA-CP-3078, pages 635–667, NASA, Cleveland, OH (Apr. 1990).

[30] Portz, R. and Segal, C., ***Penetration of Gaseous Jets in Supersonic Flows***, AIAA J., 44(10):2426–2429 (Oct. 2006).

[31] McClinton, C. R., ***Effect of Ratio of Wall Boundary-Layer Thickness to Jet Diameter on Mixing of a Normal Hydrogen Jet in Supersonic Stream***, NASA Technical Memorandum NASA TM X-3030, NASA, Hampton, VA (1974).

[32] van Leer, B., ***Towards the Ultimate Conservative Difference Scheme. V: A Second-Order Sequel to Godunov's Method***, J. Comput. Phys., 32(1):101–136 (Jul. 1979).

[33] Edwards, J. R., ***A Low-Diffusion Flux-Splitting Scheme for Navier-Stokes Calculations***, Comput. Fluids., 26(6):635–659 (Jul. 1997).

[34] McBride, B. J., Gordon, S., and Reno, M. A., ***Thermodynamic Data for Fifty Reference Elements***, NASA Technical Paper 3287/REV1, NASA, Cleveland, OH (Feb. 2001).

[35] Pulliam, T. H. and Chaussee, D. S., ***A Diagonal Form of an Implicit Approximate-Factorization Algorithm***, J. Comput. Phys., 39(2):347–363 (Feb. 1981).

[36] Menter, F. R., ***Two-Equation Eddy-Viscosity Turbulence Models for Engineering Applications***, AIAA J., 32(8):1598–1605 (Aug. 1994).

[37] Wilcox, D. C., ***Turbulence Modeling for CFD***, DCW Industries, Inc., La Cañada, CA (2000).

[38] Waitz, I., Marble, F., and Zukoski, E., ***Vorticity Generation by Contoured Wall Injectors***, in *AIAA/SAE/ASME/ASEE 28th Joint Propulsion Conference and Exhibit*, AIAA 92-3550, AIAA, Nashville, TN (Jul. 1992).

[39] Schneider, C. A., Rasband, W. S., and Eliceiri, K. W., ***NIH Image to ImageJ: 25 Years of Image Analysis***, Nat. Methods, 9(7):671–675 (Jul. 2012).

[40] Tseng, Q., ***Study of Multicellular Architecture with Controlled Microenvironment***, Ph.D. thesis, Université de Grenoble (2011).

[41] Bradski, G., ***The OpenCV Library***, Dr. Dobb's Journal of Software Tools (2000).

[42] Tecplot, Inc., ***http://www.tecplot.com/*** (2017).

[43] Palma, P. C., ***Laser-Induced Fluorescence Imaging in Free-Piston Shock Tunnels***, Ph.D. thesis, Australian National University (Feb. 1999).

[44] Luque, J. and Crosley, D. R., ***LIFBASE: Database and Spectral Simulation Program (Version 1.5)***, Tech. Rep. MP 99-009, SRI International (1999).

[45] Kolmogorov, A. N., ***The Local Structure of Turbulence in Incompressible Viscous Fluid for Large Reynolds Numbers***, Dokl. Akad. Nauk SSSR, 30(11):301–305 (1941).

[46] Pope, S. B., ***Turbulent Flows***, Cambridge University Press, Cambridge, UK (2000).

[47] Paul, P. H., Gray, J. A., Durant Jr., J. L., and Thoman Jr., J. W., ***A Model for Temperature-Dependent Collisional Quenching of NO*** $A^2\Sigma^+$, Appl. Phys. B, 57:249–259 (1993).

[48] Eckbreth, A. C., ***Laser Diagnostics for Combustion Temperature and Species***, in *Combustion Science and Technology Book Series*, vol. 3, Taylor and Francis, New York, NY, 2 edn. (1996).

[49] Danehy, P. M., Palma, P. C., Boyce, R. R., and Houwing, A. F. P., ***Numerical Simulations of Laser-Induced Fluorescence Imaging in Shock-Layer Flows***, AIAA J., 37:715–722 (1999).

[50] Danehy, P. M., Bathel, B. F., Johansen, C., Winter, M., Cutler, A. D., and O'Byrne, S., ***Molecular-Based Optical Measurement Techniques for Nonequilibrium Hypersonic Flows***, in *Hypersonic Nonequilibrium Flows*, chap. 5, AIAA (2015).

[51] Settersten, T. B., Patterson, B. D., and Carter, C. D., ***Collisional quenching of NO*** $A^2\Sigma^+(v' = 0)$ ***between 125 and 294 K***, J. Chem. Phys., 130:204302 (2009).

[52] di Rosa, M. D., ***High-Resolution Line Shape Spectroscopy of Transitions in the Gamma Bands of Nitric Oxide***, Ph.D. thesis, Stanford University (1996).

APPENDIX

PLIF is a nonintrusive laser diagnostic technique that can be used for flow visualization and quantitative measurements of velocity, species concentration, temperature, and pressure. However, to realize the quantitative aspect of LIF for one quantity, an understanding of the sensitivities to other flowfield properties or some assumptions are required. Furthermore, knowing the sensitivities is only beneficial if the additional needed flow properties can be simultaneously measured together with the quantity of interest. Such additional measurements are often only possible for point measurements and become impractical for multipoint or planar measurements, making the latter often only useful for flow visualizations. Nevertheless, because the theoretical aspects of LIF are relatively well understood,[48] models for the LIF signal (e.g., Paul et al.[47]) can be developed and applied to the CFD results to obtain a numerical approximation of LIF. The comparisons between the experimentally and numerically obtained LIF can be used in a semiquantitative manner to verify the accuracy of the CFD simulation, which can further serve as a source of other quantities of interest. Although the LIF signal is but a single quantity, it does depend on the flow velocity (in the plane of the laser sheet propagation), mixture composition, temperature, and pressure, making it a comprehensive surrogate quantity to use for verifying numerical simulations. The qualifier “semi-” is used here when discussing experimental and numerical LIF comparisons to highlight the fact that the LIF models and numerical simulations include modeling assumptions and approximations that may not always be valid.

Although a detailed discussion of the theoretical aspects of LIF is beyond the scope of this appendix, extensive material can be found in the literature.[43,44,47,48,50] Here, we limit the discussion to stating only that LIF can be described as the absorption of laser light via a resonant transition by an atom or a molecule, which leads to a modification (excitation) of the quantum-energetic configuration of that atom or molecule (or generically an absorber) from that in the ground state. The absorption of laser light is followed by a spontaneous emission of a photon (fluorescence) to return the absorber back to its ground state. This emission (fluorescence) is typically shifted to a higher wavelength (i.e., “red-shifted”) from that of the incident laser light and can be isolated using filters. The simplest model for this phenomena is a “two-level model,”[20,47] which includes the majority of LIF features under the conditions where LIF is usually applied.[43] A schematic of the two-level model for the absorber energy states is shown in Fig. 32. The ground and excited state energy configurations are denoted by 1, and 2, respectively. The processes typically considered in a two-level model are: the stimulated absorption and emission, spontaneous emission, and collisional excitation and quenching. In Fig. 32, these processes are denoted by their rate constants: W_{12} and W_{21}, A_{21}, and Q_{12} and Q_{21}, respectively, with the order of the subscripts and arrowheads denoting the process direction. The processes that represent the incoming laser light and the corresponding “red-shifted” fluorescence are the stimulated absorption and spontaneous emission, respectively. The stimulated emission process also emits photons as a result of the interactions of the incoming laser light with the electrons already populating the excited state, which then return to the ground state. However, this effect is negligible when the excited state population is small. In addition, the photons emitted by stimulated emission

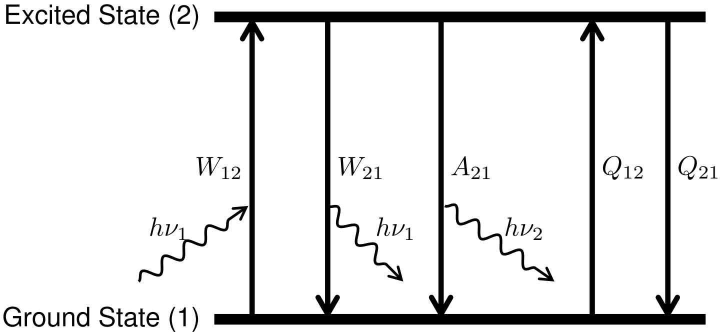

Figure 32. Two-level model of the energy levels and processes in an absorber.

process are identical in frequency to those of the incident laser light and can therefore be filtered out to isolate the fluorescence signal associated with the spontaneous emissions. The collisional excitation and quenching describe energy state changes in the absorber due to the intermolecular motion and resulting collisions in the probed medium. Of the two, the collisional excitation is negligible for transitions in the visible and ultraviolet regions.[43] The collisional quenching, however, plays a key role in determining the fluorescence quantum yield, or fluorescence efficiency.

The derivation of the two-level model, under various relevant assumptions, can be found in Palma[43] and Eckbreth.[48] Here, we use a form proposed by Paul et al.,[47] which applies in the the weak excitation (fluorescence) limit (or linear solution limit):

$$S = C_{opt} E_p \frac{\chi_{NO}\, P}{k_B T}\, \phi(P, T, \chi_\alpha) \sum_i \left(f_B(T, J)\, B_{12}(J)\, g(v_0, v_l, \delta v_l, P, T, \chi_\alpha, u_\parallel) \right)_i .^{\dagger} \tag{8}$$

This equation is the same as that already presented in the main paper (i.e., Eq. 3), with the exception that the proportionality has been explicitly replaced by a constant C_{opt}, which represents a collection of constants that describe the optical system. E_p denotes the total laser energy per pulse and all the other quantities have been previously defined. The fluorescence quantum yield, ϕ, is

$$\phi = \frac{A}{A + Q(P, T, \chi_\alpha)}, \tag{9}$$

where A is the Einstein spontaneous emission rate that is inversely proportional to the NO lifetime,[51] τ_{NO} (see Table 2), and Q is the collisional quenching rate, Q_{21}, discussed above. The latter is defined as:

$$Q(P, T, \chi_\alpha) = \sqrt{\frac{8 k_B T}{\pi m_{NO}}} \frac{P}{k_B T} \sum_\alpha^{N_s} \left(\chi_\alpha \sqrt{1 + \frac{m_{NO}}{m_\alpha}} \sigma_\alpha \right), \tag{10}$$

where the summation is over N_s species in the mixture, and m_α and σ_α are the mass and collisional cross-section of species α in the mixture, respectively. For the mixture of NO in air, the collisional cross-sections are obtained from empirical functions based on the experimental measurements of Settersten et al.:[51]

$$\begin{aligned} \sigma_{N_2}(\text{Å}^2) &= 0.008 + 2.04\, \exp(-2250/T) + 96.0\, \exp(-12700/T) \\ \sigma_{O_2}(\text{Å}^2) &= 22.5\, \exp(61.9/T) + 7.41\, \exp(-3800/T) \\ \sigma_{NO}(\text{Å}^2) &= 34.8\, \exp(48.5/T) + 13.3\, \exp(-2690/T).^{\ddagger} \end{aligned} \tag{11}$$

The collisional cross-section of helium gas is not included because helium is extremely inefficient as compared to the other mixture constituents at quenching NO fluorescence. The consequence of this is that the collisional quenching is zero and the fluorescence yield is unity in the limit of pure helium gas. However, in this limit, the mole fraction of NO is also zero, producing the correct result of no fluorescence. With the expressions in Eqs. 10 and 11, the collisional quenching rate is a linear function of the pressure and composition, and a nonlinear function of the temperature. As a result, the fluorescence quantum yield, ϕ, decreases with increasing pressure but has a more complex, monotonically increasing profile with increasing temperature.

The first term inside the summation of Eq. 8 is the Boltzmann fraction. This quantity describes the probability that an absorber will be found in a certain energy state among all allowable energy states, as a function of the temperature and the rotational quantum number, when a system is in thermodynamic equilibrium.

[†] In the work of Ivey et al.,[20] this equation appears incorrect or applicable only in the limit of equal molecular weights for the mixture constituents. This is because, in an attempt to recast the $\chi_{NO} P/k_B T$ term in terms of the flow density, instead of the number density, using ideal gas equation of state, Ivey et al.[20] mistakenly retained the mole fraction, χ_{NO}, instead of using the mass fraction, Y_{NO}.

[‡] In the work of Ivey et al.,[20] this equation is copied from Settersten et al.[51] with errors.

Formulations that include corrections for thermodynamic nonequilibrium effects are also available.[43] The Boltzmann fraction is given by the Boltzmann expression:[48]

$$f_B(T, J) = \frac{hc}{k_B T} B_v (2J + 1)\, \exp\left(-B_v J(J + 1)\frac{hc}{k_B T}\right), \tag{12}$$

where h is the Planck's constant, c is the speed of light, and B_v is the effective rotational constant:[48]

$$B_v = B_e - \alpha_e (v + 1/2), \tag{13}$$

with B_e, α_e, and v corresponding to the equilibrium rotational constant, vibrational-rotational interaction constant, and the vibrational quantum number of the transition, respectively. The former can be computed from:

$$B_e = \frac{h}{8\pi^2 c\, I_e}, \tag{14}$$

where I_e is the equilibrium moment of inertia of NO obtained from:

$$I_e = \frac{m_N\, m_O}{m_N + m_O} r_e^2, \tag{15}$$

where m_N, and m_O are the mass of the N and O atoms, respectively, and r_e is the equilibrium radius of NO. The constants needed to evaluate the above quantities numerically have been tabulated in Table 2 for reference. In addition, Eq. 12 has been plotted as a function of temperature for several values of the rotational quantum number relevant to the current experiments in Fig. 33, where the different numbers in the legend denote the rotational quantum numbers and the figure's inset offers a focus on the lower range of the temperature.

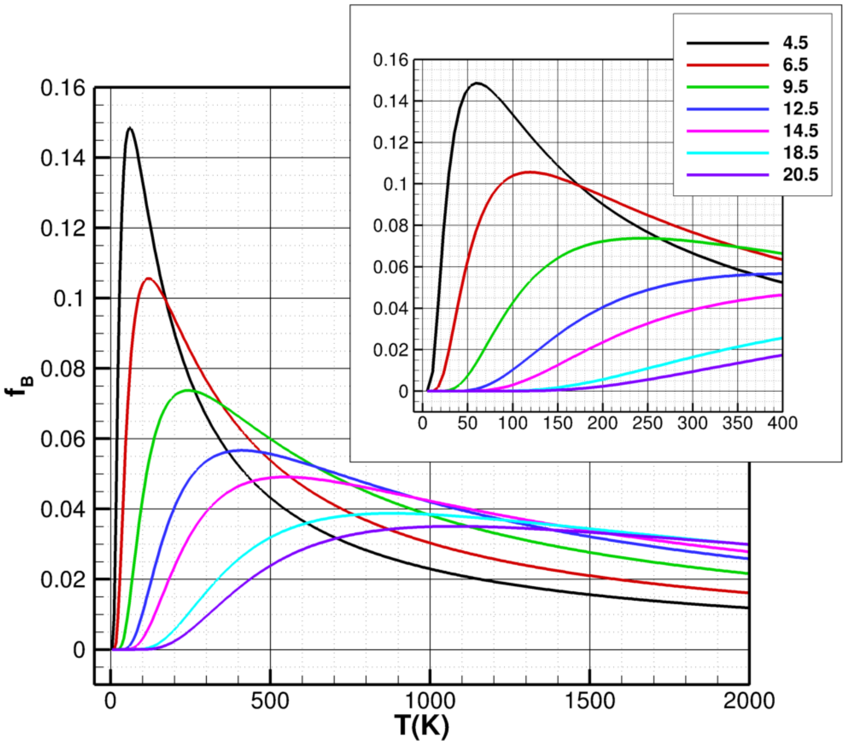

Figure 33. Plot of Boltzmann fraction vs. temperature for several values of rotational quantum number.

The next term in the summation of Eq. 8 is the Einstein absorption coefficient, which represents the rate of stimulated absorption. This coefficient depends on the rotational quantum number of the transition and was obtained using the LINUS code[43] developed at the Australian National University. The values for the Einstein absorption coefficient are tabulated in Table 3 for the transition lines probed in the current experiments. In addition, the table contains each transition line's center absorption wavenumber in a vacuum, the laser center wavenumber (to indicate laser tuning), and the laser FWHM. The latter three values are needed to compute the spectral overlap integral, which is the last term inside the summation of Eq. 8. This term accounts for the spectral interactions between the laser beam and the transition lines being probed, and is important because neither the laser profile nor the transition lines are spectrally monochromatic. These interactions are modeled using a convolution integral over the wavenumber space between the spectral profile of the laser beam, usually Gaussian or Lorentzian, and the spectral profile or profiles corresponding to the transition lines being probed. The spectral width and profile shape of the laser beam can be somewhat controlled via the experimental setup. The width and profile of the transition lines depend on at least two key physical effects: Doppler and pressure (collision) broadening. The Doppler broadening increases the spectral width of the transition line profile due to the thermal motions of the atoms or molecules, and it is described using a Gaussian profile[48] with the FWHM proportional to the square root of the temperature. The collision broadening increases the width of the transition line via periodic interruptions to the absorption or emission processes due to the inter-molecular collisions.[48] The resulting profile is Lorentzian. The general expression for the spectral overlap convolution integral is:

$$g(v;\, v_0, v_l, \Delta v_l, P, T, \chi_\alpha, u_\parallel) = \int\limits_{-\infty}^{+\infty} \mathrm{d}v'\, g_l(v'-v;\, v_l, \Delta v_l) \int\limits_{-\infty}^{+\infty} \mathrm{d}v''\, g_d(v''-v';\, v_0, T, u_\parallel)\, g_c(v'';\, v_0, P, T, \chi_\alpha), \quad (16)$$

Table 2. Constants used in the current PLIF modeling approach.

Property	Symbol	Formula	Value	Units
Avogadro's number	N_a		$6.022140857 \times 10^{26}$	$atoms/kmole$
Universal gas const.	R_u		$8.314459848 \times 10^{3}$	$J/(kmole\,K)$
Boltzmann const.	k_B	$\frac{Ru}{Na}$	$1.38064852 \times 10^{-23}$	$(m^2\,kg)/(s^2\,K)$
Speed of light	c		$2.997924580 \times 10^{8}$	m/s
Planck const.	h		$6.62607004 \times 10^{-34}$	$(m^2 kg)/s$
Molecular weight of oxygen	w_O		15.9994	$kg/kmole$
Molecular weight of nitrogen	w_N		14.00674	$kg/kmole$
Molecular weight of helium	w_{He}		4.002602	$kg/kmole$
Mass of oxygen atom	m_O	$\frac{w_O}{N_a}$	$2.656762832 \times 10^{-26}$	$kg/atom$
Mass of nitrogen atom	m_N	$\frac{w_N}{N_a}$	$2.325873860 \times 10^{-26}$	$kg/atom$
Mass of helium atom	m_{He}	$\frac{w_{He}}{N_a}$	$6.646476884 \times 10^{-27}$	$kg/atom$
Mass of nitric oxide molecule	m_{NO}	$m_O + m_N$	$4.982636692 \times 10^{-26}$	$kg/molecule$
Mass of oxygen gas molecule	m_{O_2}	$2m_O$	$5.313525665 \times 10^{-26}$	$kg/molecule$
Mass of nitrogen gas molecule	m_{N_2}	$2m_N$	$4.651747720 \times 10^{-26}$	$kg/molecule$
Equilibrium radius of NO	r_e		1.150725×10^{-10}	m
Equilibrium moment of inertia for NO	I_e	$\frac{m_N m_O}{m_N + m_O} r_e^2$	$1.642187794 \times 10^{-46}$	m^2
Equilibrium rotational const. for NO	B_e	$\frac{h}{8\pi^2 c I_e}$	170.4601	$1/m$
Vibrational-rotational interaction const.	α_e		1.78	$1/m$
Effective rotational const. for NO	B_v	$B_e - \alpha_e(v + 1/2)$	169.5701	$1/m$
Vibrational quantum number of the transition	v		0	
NO lifetime	τ_{NO}		192.0	ns

where g_l, g_d, and g_c are the laser spectral profile, and the Doppler and collision broadening profiles, respectively, and the integral is evaluated over the entire spectrum. In the current analysis, the laser spectral profile is assumed to be Gaussian, in the form:

$$g_l(v;\, v_l, \Delta v_l) = \sqrt{\frac{4\ln(2)}{\pi \Delta v_l^2}}\, \exp\left(-4\ln(2)\frac{(v - v_l)^2}{\Delta v_l^2}\right), \tag{17}$$

where v_l and Δv_l are the laser center wavenumber and FWHM linewidth, respectively. Evaluating the above integral at a wavenumber of zero, produces an overlap fraction between the laser spectral profile and the profiles of the broadening processes. Furthermore, the convolution of the Gaussian profile due to the Doppler broadening and the Lorentzian profile due to the pressure (or collision) broadening (i.e., second integral above) produces a Voigt profile, which under certain circumstances can be approximated by a Gaussian profile.[48] Such an approximation can be exploited to obtain an analytic solution of Eq. 16 because the convolution of two Gaussian functions is also Gaussian. Figure 34 shows a comparison between Gaussian and Voigt profiles with the same FWHM for several values of the Voigt constant, *a*. It can be observed that for Voigt constant values of up to about 0.5, a Gaussian profile is a good approximation of the Voigt profile. For values of the Voigt constant greater than about 0.5, the consequence of the Gaussian assumption is that contributions from the broadened transition lines near the “tails” of the Voigt profile are “clipped” by a comparable Gaussian profile. Figure 35 shows the contour plot of the Voigt constant on a streamwise plane through the center of the strut injector computed from the CFD simulations. The contours show that the value of Voigt constant is almost everywhere less than 0.5, suggesting that a Gaussian assumption is reasonable for the current experiments. With the Gaussian assumption, the solution to Eq. 16 becomes:[20]

$$g = \sqrt{\frac{4\ln(2)}{\pi(\Delta v_l^2 + \Delta v_d^2 + \Delta v_c^2)}}\, \exp\left(-4\ln(2)\frac{(\delta v_l + \delta v_d + \delta v_c)^2}{\Delta v_l^2 + \Delta v_d^2 + \Delta v_c^2}\right), \tag{18}$$

where δv_l, δv_d, and δv_c are the laser detuning (i.e., $v_l - v_0$,), and Doppler and collision shifts from the transition line center absorption wavenumber, respectively; and Δv_l, Δv_d, and Δv_c correspond to the FWHM of the laser linewidth, and Doppler and collision broadening, respectively.

The amount of laser detuning can be controlled experimentally by carefully “tuning” the laser to a desired transition line. Similarly, the laser FWHM linewidth can be controlled and measured experimentally. In the current analysis, no detuning is assumed with respect to the target transition line, and the measured laser FWHM are reported in Table 3. The expressions for the Doppler shift and FWHM of broadening are known exactly, and can be found in Eckbreth.[48] Here, they are repeated for completeness:

$$\delta v_d = \frac{v_0\, u_\parallel}{c}, \tag{19}$$

$$\Delta v_d = \frac{2v_0}{c}\sqrt{\frac{2\ln(2) k_B T}{m_{NO}}}. \tag{20}$$

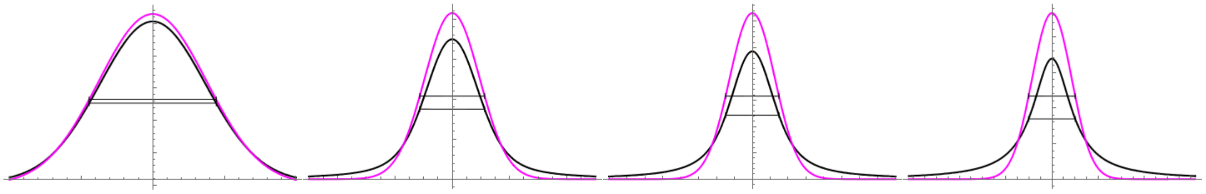

(a) *a*=0.1 (b) *a*=0.5 (c) *a*=1.0 (d) *a*=10.0

Figure 34. Comparison between the Gaussian (magenta) and Voigt (black) profiles having the same FWHM (denoted by horizontal lines) for increasing values of the Voigt constant, *a*.

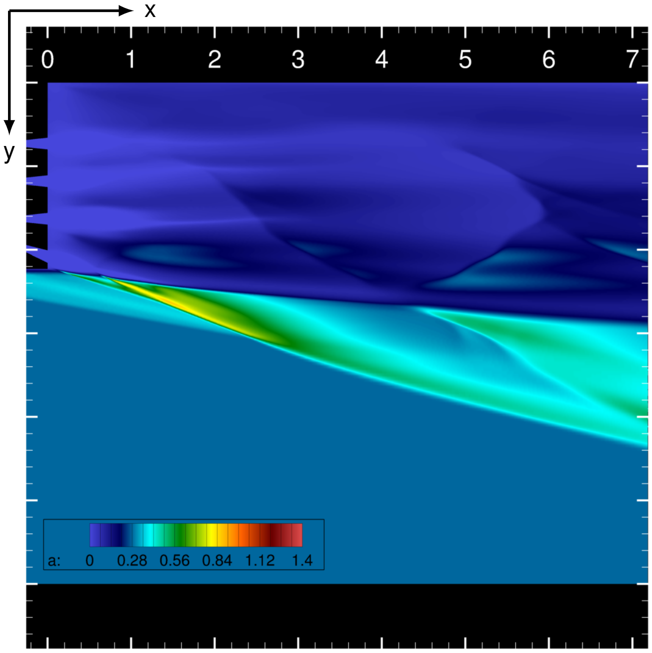

Figure 35. Contour plot for the Voigt constant, *a*, on a streamwise plane through the center of the strut injector.

Table 3. Spectroscopic constants used in the current PLIF modeling approach.

Line:	$^{S}R_{21}(9.5)$	$Q_1(20.5)$	$^{Q}P_{21}(20.5)$	$R_2(18.5)$
J[†]	9.5	20.5	20.5	18.5
$B_{12}\,(cm^2/(cm\,J))$[‡]	69.34	293.205	44.473	128.108
$v_0\,(1/cm)$[§]	44295.4531	44296.5328	44296.5877	44294.6227
$v_l\,(1/cm)$[¶]	44295.4531			
$\Delta v_l\,(1/cm)$[‖]	2.0			
Line:	$^{O}P_{12}(6.5)$	$^{O}P_{12}(14.5)$		
J	6.5	14.5		
$B_{12}\,(cm^2/(cm\,J))$	99.669	67.697		
$v_0\,(1/cm)$	44056.3514	44055.8208		
$v_l\,(1/cm)$	44056.3514[**]			
$\Delta v_l\,(1/cm)$	0.2			
Line:	$^{R}Q_{21}(12.5)$	$R_1(12.5)$		
J	12.5	12.5		
$B_{12}\,(cm^2/(cm\,J))$	127.384	132.29		
$v_0\,(1/cm)$	44279.4455	44279.4093		
$v_l\,(1/cm)$	44279.4455			
$\Delta v_l\,(1/cm)$	0.2			

[†] Rotational quantum number

[‡] Einstein B absorption coefficient. From LINUS

[§] Transition line center absorption wavenumber. From LINUS

[¶] Laser center wavenumber

[‖] Laser FWHM

[**] CFI images have been computed by "tuning" the laser to the 14.5 line.

The correlations for the pressure shift and broadening are obtained from di Rosa:[52]

$$\delta v_c(1/cm) = \frac{P}{101325}\left(-0.18\chi_{N_2}\left(\frac{295}{T}\right)^{0.50} - 0.159\chi_{O_2}\left(\frac{295}{T}\right)^{0.52} - 0.167\chi_{NO}\right), \tag{21}$$

$$\Delta v_c(1/cm) = \frac{P}{101325}\left(0.585\chi_{N_2}\left(\frac{295}{T}\right)^{0.75} + 0.527\chi_{O_2}\left(\frac{295}{T}\right)^{0.66} + 0.551\chi_{NO}\right), \tag{22}$$

where pressure and temperature are specified in units of Pa and K, respectively. The contributions to the pressure shift and broadening due to the presence of helium in the mixture are neglected in the present work.